

Anomalous Behavior of the Dielectric and Pyroelectric Responses of Ferroelectric Fine-Grained Ceramics

Oleksandr S. Pylypchuk¹, Serhii E. Ivanchenko², Mykola Y. Yelisiiev^{1,3}, Andrii S. Nikolenko^{1,3}, Victor I. Styopkin¹, Bohdan Pokhylko², Vladyslav Kushnir², Denis O. Stetsenko¹, Oleksii Bereznykov¹, Oksana V. Leschenko², Eugene A. Eliseev², Vladimir N. Poroshin¹, Nicholas V. Morozovsky^{1*}, Victor V. Vainberg^{1†}, and Anna N. Morozovska^{1‡}

¹ Institute of Physics, National Academy of Sciences of Ukraine,
46, pr. Nauky, 03028 Kyiv, Ukraine

² Frantsevich Institute for Problems in Materials Science, National Academy of Sciences of Ukraine
Omeliana Pritsaka str., 3, Kyiv, 03142, Ukraine

³ Lashkarev Institute of Semiconductor Physics, National Academy of Sciences of Ukraine,
41, pr. Nauky, 03028 Kyiv, Ukraine

Abstract

We revealed the anomalous temperature behavior of the giant dielectric permittivity and unusual frequency dependences of the pyroelectric response of the fine-grained ceramics prepared by the spark plasma sintering of the ferroelectric BaTiO₃ nanoparticles. The temperature dependences of the electro-resistivity indicate the frequency-dependent transition in the electro-transport mechanisms between the lower and higher conductivity states accompanied by the maximum in the temperature dependence of the loss angle tangent. The pyroelectric thermal-wave probing revealed the existence of the spatially inhomogeneous counter-polarized ferroelectric state at the opposite surfaces of the ceramic sample. We described the anomalous temperature behavior of the giant dielectric response and losses using the core-shell model for ceramic grains and modified Maxwell-Wagner approach. We assume that core shells and grain boundaries, which contain high concentration of space charge carriers due to the presence of graphite inclusions in the inter-grain space, can effectively screen weakly conductive ferroelectric grain cores. The superparaelectric-like state with a giant dielectric response can appear in the paraelectric shells and inter-grain space due to the step-like thermal activation of localized polarons in the spatial regions, agreeing with experimentally observed frequency-dependent transition of the electro-transport mechanism. The obtained results can be the key for the description of complex electrophysical properties inherent to the strongly inhomogeneous

* corresponding author, e-mail: nicholas.v.morozovsky@gmail.com

† corresponding author, e-mail: viktor.vainberg@gmail.com

‡ corresponding author, e-mail: anna.n.morozovska@gmail.com

media with electrically coupled insulating ferroelectric nanoregions and semiconducting super paraelectric-like regions.

I. INTRODUCTION

The barium titanate (BaTiO_3) is a classical ferroelectric material [1], whose ceramics are widely used for a variety of applications, such as positive temperature coefficient thermistors, (ferroelectric resistors), pyroelectric detectors [2] and multilayer ceramic capacitors (**MLCC**) [3]. The problem of BaTiO_3 (**BTO**) application to ceramic capacitors requires high relative dielectric permittivity values, as high as 10^5 , and is closely connected to the problem of the fine-grained BTO ceramics sintering and production. Traditional hot-pressing sintering (**HPS**) technologies, which use relatively high sintering temperatures (from 1200 to 1450 °C) and times (2 to 5 hours), result in BTO ceramics with a relative density of about 80% and developed granular structure. However, resulting dielectric parameters of HPS BTO ceramics are not enough for MLCC applications.

In accordance with modern requirements, it is desirable to minimize the energy consumption and time of the ceramic sintering procedure. These requirements can be fulfilled using the spark plasma sintering (**SPS**) method [4, 5, 6], which allows to obtain colossal and frequency stable permittivity of BTO nanoceramics [7], has been adapted for the product manufacturing [8] and mass production [6]. SPS allows to achieve high density and suppression of ceramic grain growth [9, 10]. In particular, the mechanical activation synthesis and SPS at 1112°C for 3 minutes under 50 MPa leads to the BTO nanoceramics with relative density of 98%, which dielectric constant is as high as $3.5 \cdot 10^5$ and loss angle tangent is about 0.07 at the frequency of 1 kHz [7].

The SPS is superior to the HPS in terms of the temperature control, the control quality of grain boundaries and fine-crystalline structure. However, the SPS uses an electrical current between particles placed in a graphite die. The presence of the conducting graphite inclusions, which concentration changes from the ceramic pellet surface towards its depth, can influence strongly on the electrophysical properties of the ceramics. Often the surface layer with the highest concentration of graphite inclusions is eliminated as contamination.

In this work we show that the graphite inclusions, which are inevitably present in the inter-grain space of the SPS BTO ceramics, can play an important role in the appearance of the superparaelectric-like state being the main reason of its giant dielectric response. We revealed the anomalous temperature behavior of the giant dielectric permittivity and unusual frequency dependences of the pyroelectric response of the ferroelectric fine-grained ceramics prepared by SPS of the BTO nanoparticles with the average size of 25 nm. We described the anomalous plateau-like giant dielectric response using the core-shell model for ceramic grains and the Maxwell-Wagner approach [11] for inhomogeneous semiconducting media. The cores are weakly conductive; their shells and

grain boundaries are semiconducting with a high concentration of space charge carriers in the presence of graphite inclusions in the inter-grain space. Within the proposed model the superparaelectric-like state exists in the shells, which cover ferroelectric cores of the grains. The superparaelectric-like state with a giant dielectric response appears due to the thermal activation of localized polarons [12].

The paper is structured as follows: **Section II** contains the experimental results and their theoretical analysis; and **Section III** contains a summary. The details of samples characterization are listed in **Supplemental Materials** [13].

II. EXPERIMENTAL RESULTS AND THEIR THEORETICAL ANALYSIS

We studied the polar, dielectric and pyroelectric properties in the BTO ceramics prepared by the HPS at 1250 °C at sintering time 5 hours, and the BTO ceramics prepared by the SPS at 1100 °C for 5 minutes, the heating rate is 400°C/minute. For both ways of sintering, we used the same BTO nanoparticles with the average size of 25 nm. The silver (or indium) contacts were made using the method of thermal evaporation in the vacuum deposition aggregate VUP-5M.

A. Raman and SEM Studies

The Raman spectra of the BTO ceramics prepared by the HPS are shown in **Fig. 1**. The HPS BTO ceramics exhibits five Raman-active phonon modes located at 185, 258, 307, 519 and 718 cm^{-1} and four dips located at 180, 297, 457 and 680 cm^{-1} . The mode positions are close to those known for calcined BTO nanopowders (185, 260, 306, 515 and 715 cm^{-1}) [7] and BTO-Ag nanocomposites (180, 260, 300, 514 and 712 cm^{-1}) [14]. Similar to Ref.[7], we regard that the Raman peaks at 180, 258 and 519 cm^{-1} correspond to the cubic phase of BTO, and the peaks at 307 and 718 cm^{-1} correspond to the tetragonal phase of BTO. Pronounced shape asymmetry of the 519 cm^{-1} peak can be associated with overlapping of true $A_1(\text{TO})$ and $E(\text{TO})$ modes.

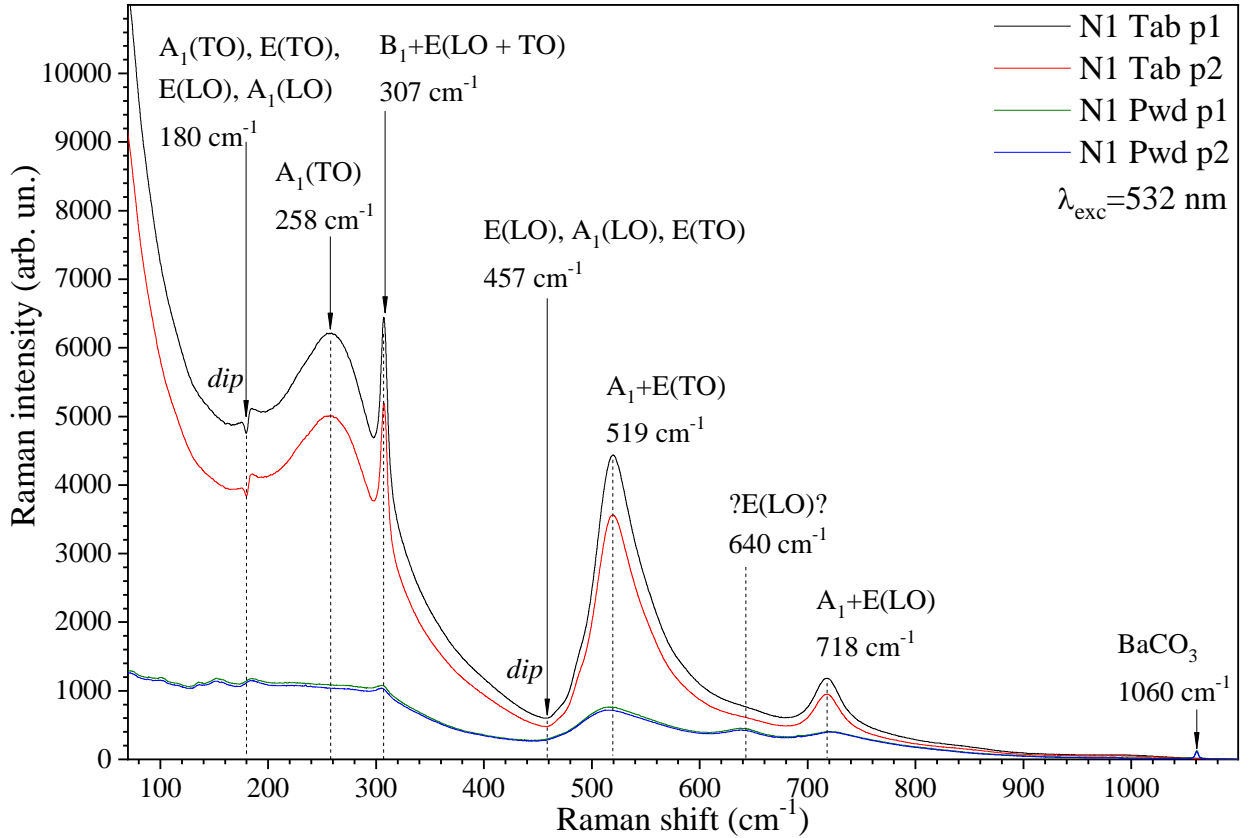


FIGURE 1. Raman spectra of the BTO ceramics prepared by the HPS.

The scanning electron microscopy (SEM) images of the SPS ceramics revealed that the number of graphite inclusions (shown by black spots in **Fig. 2(a)**) decreases in two times from the surface towards the middle of the pellet (see **Appendix A** [13] for details). According to SEM observations we prepared several samples from the SPS ceramic pellet for further studies, shown in **Fig. 2(b)**, where different samples have different concentrations of the graphite inclusions. The whole pellet has dimensions $6.2 \times 5.6 \times 2.4 \text{ mm}^3$, the dimensions of the sample # 1 are $5.6 \times 2.6 \times 2.0 \text{ mm}^3$, and the three thin slices with high and low concentrations of graphite inclusions, designated as the samples # 2, 3, and 4, have dimensions $4.5 \times 2.0 \times 0.2 \text{ mm}^3$.

The Raman spectra of the BTO ceramics prepared by the SPS and recorded in different points p1-p9 of the prism-shaped sample are shown in **Fig. 2(c)** and **2(d)**. The Raman spectra of the SPS BTO ceramics are very similar to those of HPS ceramics: one can see five Raman-active phonon modes located at 183, 258, 307, 519 and 718 cm^{-1} and four dips located at 180, 297, 457 and 680 cm^{-1} (compare with **Fig. 1**). However, the Raman spectra of the SPS BTO ceramics contains the carbon bands D (1330 cm^{-1}) and G (1610 cm^{-1}), which are clearly seen for p5, p5' and p8 points in **Fig. 2(d)** corresponding to the dark spots.

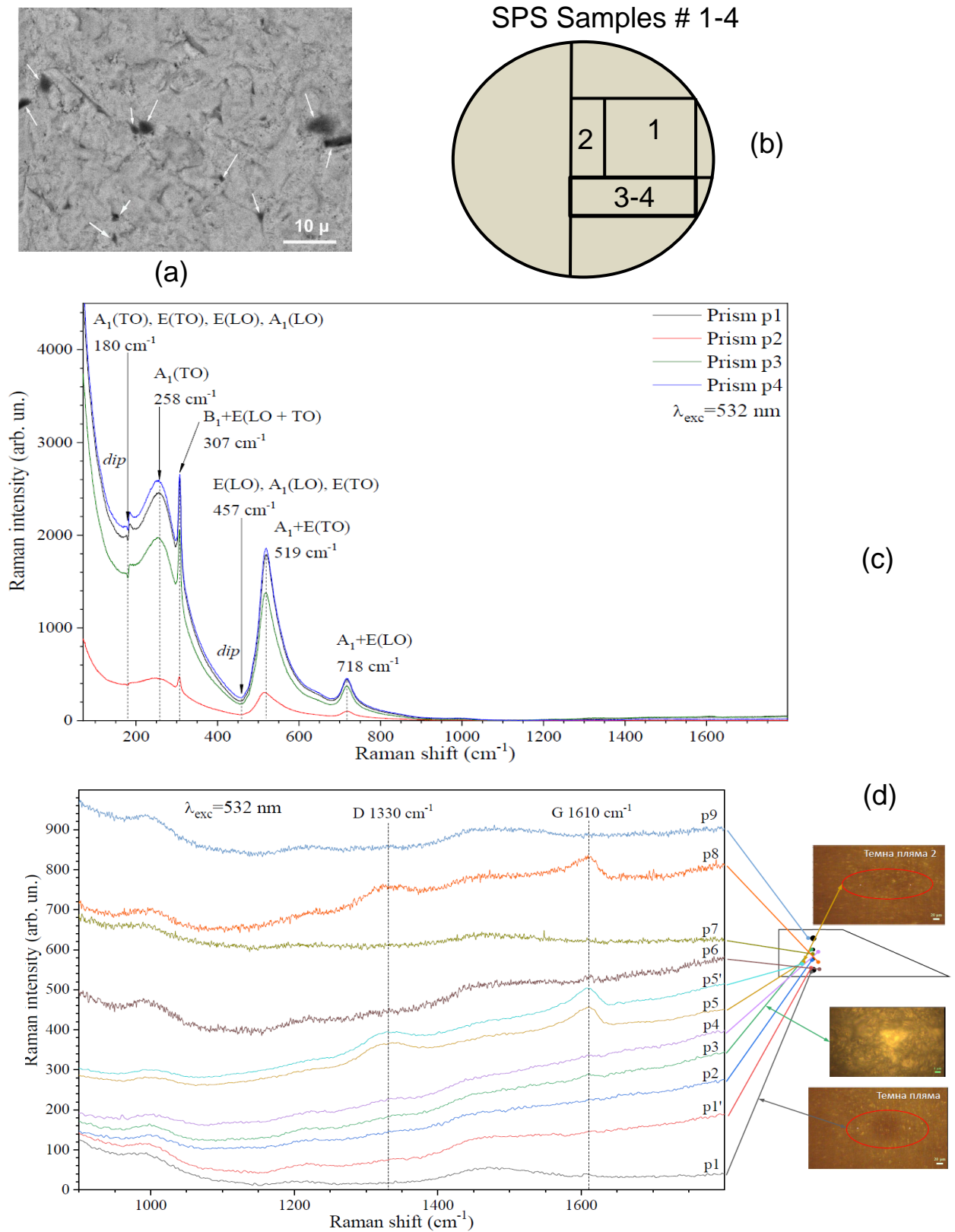


FIGURE 2. (a) Z-contrast SEM images of the SPS pellet edge. White arrows point on the black graphite inclusions. (b) Cutting diagram of the SPS BTO pellet. (c) Raman spectra of the BTO ceramics prepared by the SPS. (d) The part of the Raman spectra (c) recorded in different points p1-p9 of the prism-shaped sample of the SPS BTO ceramics (as shown in the right).

B. Dielectric Permittivity and Losses

The temperature dependences of the dielectric permittivity (ϵ) and loss tangent ($tg\delta$) of the HPS BTO ceramic pellet are shown in **Fig. 3**. It is seen that the permittivity, measured at 1, 10 and 100 kHz, has a sharp peak at approximately 125°C, which corresponds to the paraelectric-ferroelectric phase transition temperature in a bulk BTO single-crystal, and a relatively smooth maxima at about 20°C, which corresponds to the orthorhombic-tetragonal phase transition temperature and is also close to the corresponding transition temperature in a bulk BTO single-crystal. The position and value of the dielectric permittivity maximum are almost frequency-independent. The losses have a relatively sharp minima at 125°C, and a pronounced maximum at 20°C. The temperature behavior is typical for the dense HPS BTO ceramics with ferroelectric grains.

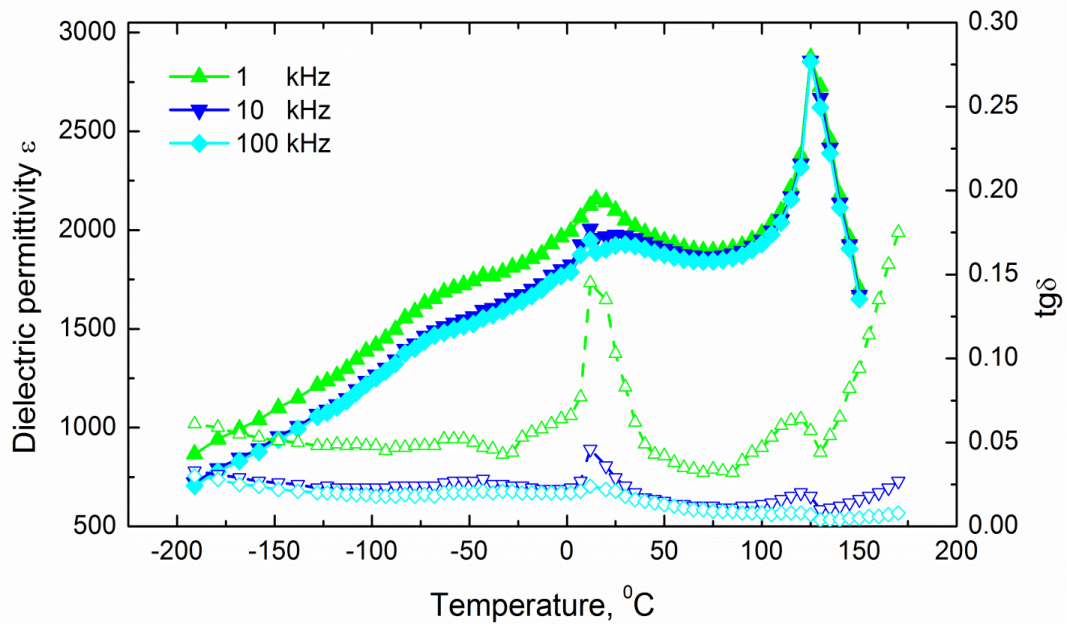


FIGURE 3. The temperature dependences of the dielectric permittivity (ϵ , filled symbols) and the dielectric losses ($tg\delta$, empty symbols) of the BTO ceramics prepared by the HPS.

The temperature dependences of the dielectric permittivity for the SPS samples # 1 - 4 are shown in **Fig. 4(a) - 4(d)**, respectively. The permittivity, measured at frequencies from 100 Hz to 100 kHz, has no pronounced maxima in the studied temperature range. Instead, the dielectric permittivity increases very strongly (by 4 orders of magnitude) under the temperature increase from -200°C to +100°C. The increase rate is the highest between -150°C and -50°C when the permittivity reaches the values $\sim (2 - 8) \cdot 10^5$, then the increase rate becomes much slower due to the permittivity saturation. The pronounced permittivity saturation appears above -75°C (for 100 Hz, 120 Hz and 1 kHz), above -50°C (for 10 kHz) and above +25°C (for 100 kHz). The slow increase of the dielectric permittivity (instead of the saturation) is observed above +75°C at 1 kHz; other curves continue to saturate in the studied temperature range. The temperature and frequency dependences of the dielectric permittivity

for the samples # 1 - 4 are qualitatively similar. The main quantitative differences are in the increase rate and saturation values of the dielectric permittivity, which can vary by one order of magnitude.

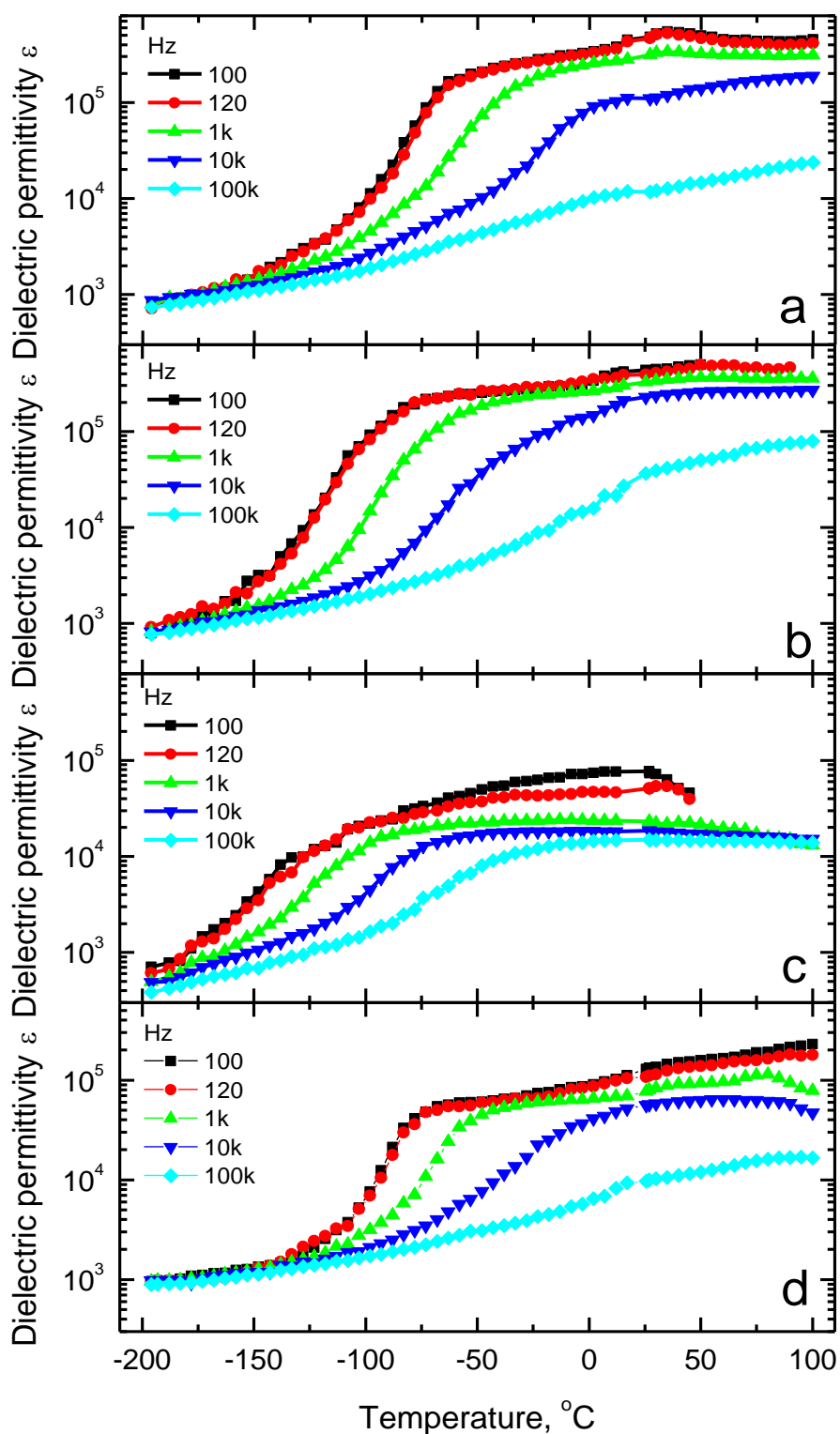


FIGURE 4. The temperature dependences of the dielectric permittivity measured for the samples # 1 (a), #2 (b), #3(c) and #4 (d) at frequencies from 100 Hz to 100 kHz.

The temperature dependences of the loss angle tangent measured for the SPS samples # 1 - 4 are shown in **Fig. 5(a) - 5(d)**, respectively. The temperature dependence of the dielectric loss angle

tangent is non-monotonic for all considered frequencies, with relatively sharp maxima at -150°C (for 100 Hz, 120 Hz and 1 kHz), -100°C (for 10 kHz) and a wide peak at -25°C (for 100 kHz). The temperature positions of the maxima are located in the middle of the region, where the dielectric permittivity increases rapidly. For the temperatures above the maximum, the losses start to increase with the temperature increase rapidly (for 100 and 120 Hz) or more slowly (for 1 kHz). We associate the increase with the likely thermal breakdown. The increase (and thus the breakdown) is absent (or occur at much high temperatures outside the studied range) for 10 kHz and higher frequencies.

For most samples (#1, 2 and 4) the maximum of $tg\delta$ shifts to the higher temperatures and its height very slightly increases with the frequency ω increase from 100 Hz to 100 kHz. We observed $tg\delta \sim \omega^{\alpha}$, where α is a small positive number. Since the performed measurements correspond to the parallel equivalent measurement connection circuit, $tg\delta \sim 1/\omega CR$, we may suggest the resulting experimental integral frequency dependence of $tg\delta$ to be determined by a complicated mixture of connections and dependences of the dielectric permittivity and resistivity of sintered particles.

The maximum in the temperature dependence of the $tg\delta$ is a reliable sign of a change in the mechanism of the electrical transport and the dielectric response of the sample. Active losses caused by the release of energy on the active part of the resistance in this area do not increase, but the reactive component, which is a combination of the capacitances (\sim permittivities) of the components forming the sample volume, changes sharply. In result the ratio of the active and reactive components also changes sharply leading to the maximum in the loss angle tangent. Thus, the maximum of the loss tangent accompanying the sharp decrease or increase in the dielectric permittivity is a fingerprint of the electrical transport mechanism change entire the sample volume.

The temperature and frequency dependences of the losses for the samples # 1, 2 and 4 are qualitatively similar. The main quantitative differences are in the positions of the loss angle tangent maximum, and the value of losses in their maximum. The breakdown can occur at frequencies below 10 kHz. Let us underline, that the sample # 3, where $tg\delta$ has no maxima, reveals the lowest resistivity and the lowest dielectric permittivity, less than 10^5 , in the high temperature range. Also, the sample has the highest losses among the all studied samples, which become very high starting from the lowest temperature. This behavior can be related with the sharp changes of polarizability at high concentration of the graphite contamination in the surface part of the pellet.

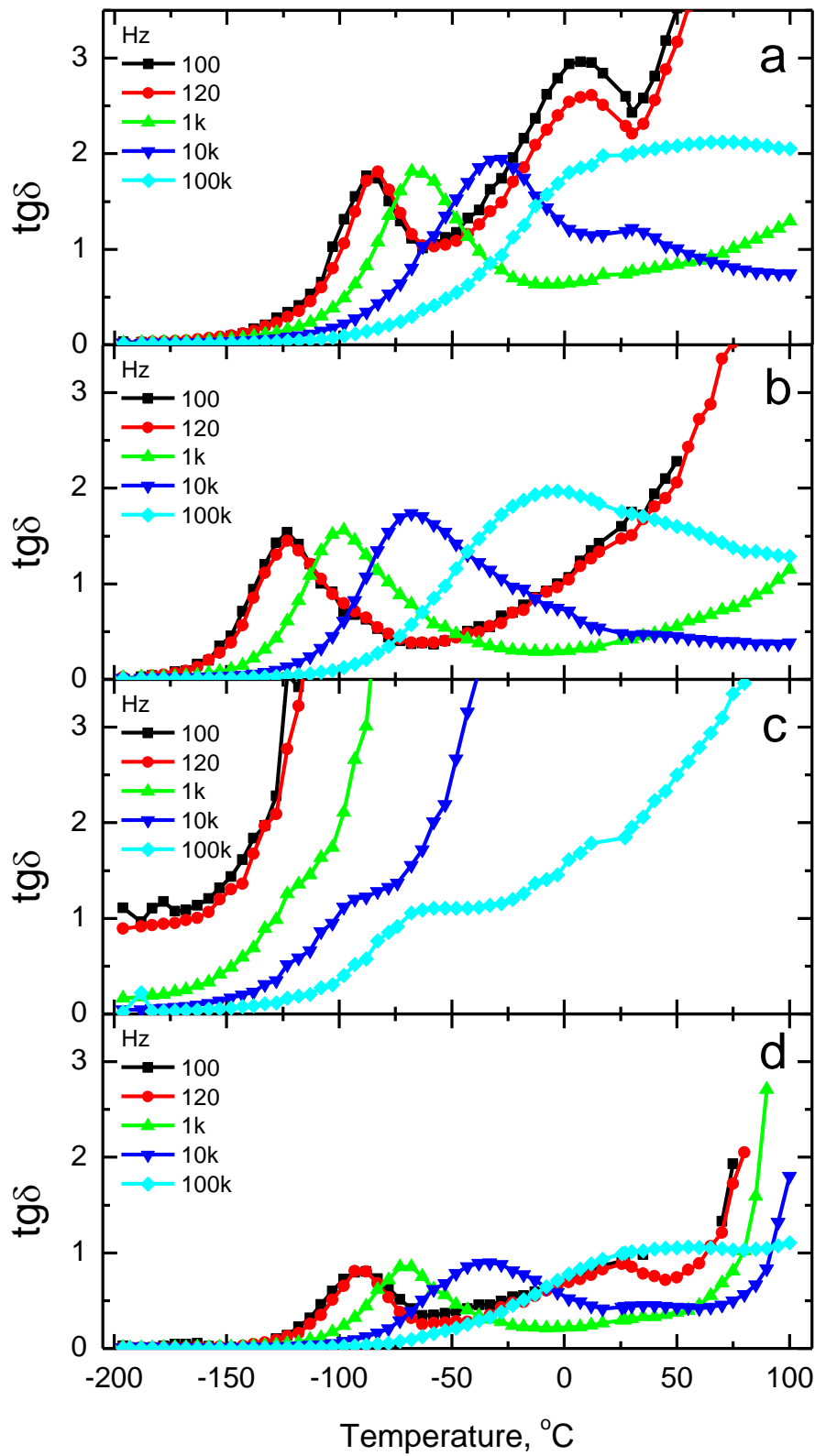


FIGURE 5. The temperature dependences of the loss angle tangent measured for the samples # 1 (a), #2 (b), #3(c) and #4 (d) at frequencies from 100 Hz to 100kHz.

Note that we show in **Figs. 4 - 5** the dielectric response measured in the temperature range from -200°C to + 100°C, which contains all significant changes of the response. The measurements

performed in a wider temperature range (namely, from -200°C to $+200^{\circ}\text{C}$), using silver pressing contacts, do not add any new information in comparison with **Figs. 4 - 5**.

C. Electric Transport Characteristics

Shown in **Fig. 6** are the temperature dependences of resistivity of the SPS samples # 1-4 measured in the direct current (DC) regime in the range from the room down to liquid nitrogen temperature. It is seen that the dependences have activation kind behavior in the Arrhenius coordinates with the activation energies in the range of 120 to 290 meV. Such a behavior with high activation energies characterizes conduction as semiconducting kind and agrees well with the model of the small polaron hopping conduction mechanism [15, 16, 17]. The activation energy in this case corresponds to the barrier height required to overcome the reaction of polarized ambient accompanying the moving charge carriers in the solid.

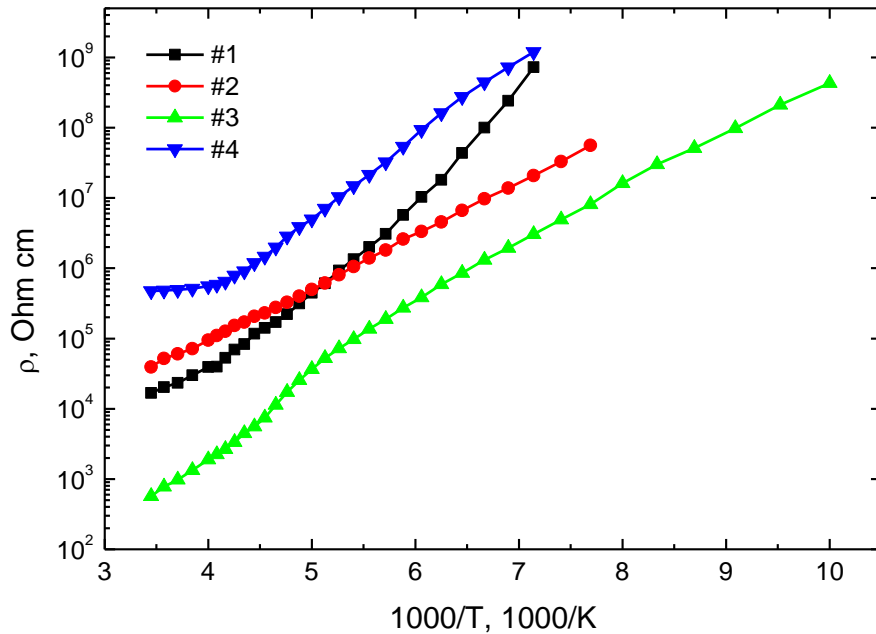


FIGURE 6. The temperature dependences of the resistivity measured for the samples # 1, 2, 3 and 4 under the small electric field strength that does not heat the charge carriers.

The polaron hopping conduction with a strong temperature dependence of resistivity applies a specific character on conduction in strong electric fields. Also, measurements of the DC current vs time have shown that all samples (more or less) are subjected to the Joule heating under the increase of applied DC voltage. It is illustrated for the sample #3 in **Fig. 7(a)**, where the temporal dependences of the relative current through the sample are shown at different applied voltages. To avoid the Joule heating, the current-voltage characteristics (I-V curves) were measured in the pulsed regime with the voltage pulse duration no more than 1 ms. The I-V curves at four temperatures for the sample #3 are shown in **Fig. 7(b)**. The I-V curves are slightly superlinear, though do not intercept even at the electric

field strength up to 2 kV/cm. This indicates that the applied electric fields are still too small to affect the energy barriers determining the conduction mechanisms. The samples #1, 2 and 4 demonstrate a similar behavior.

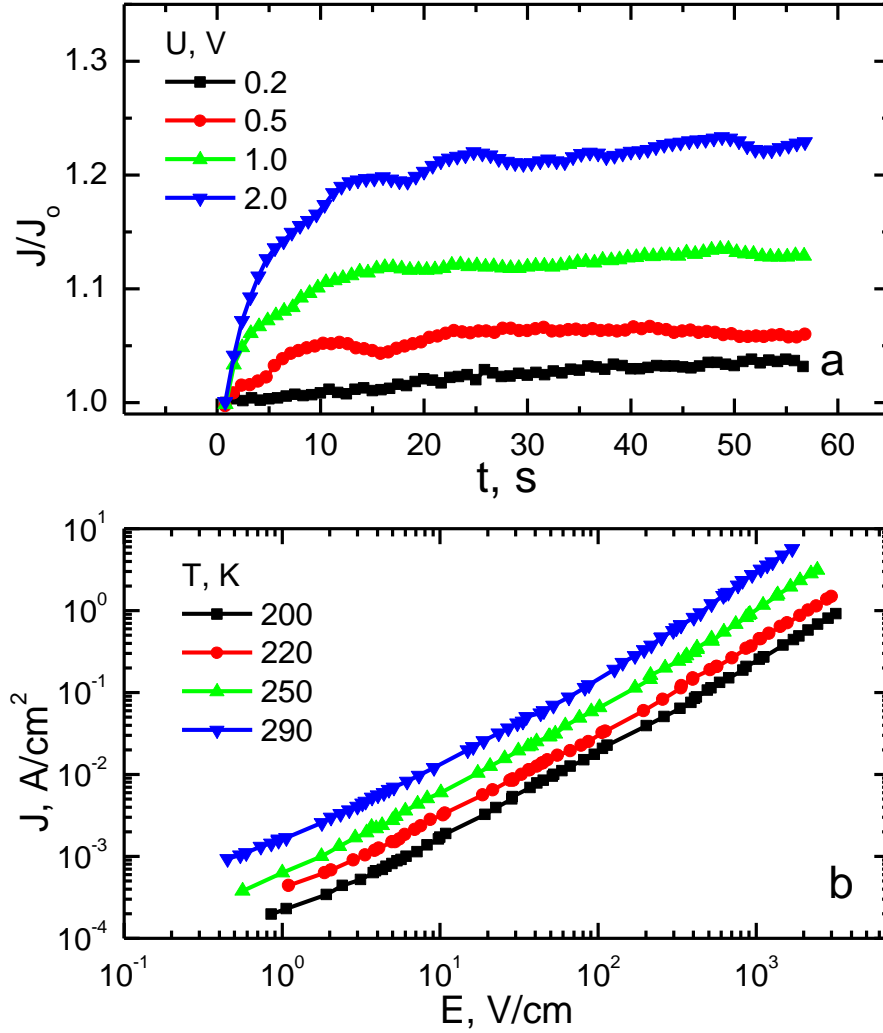


FIGURE 7. (a) Temporal dependences of the relative current through the sample at different applied voltages. (b) Current-voltage characteristics of the sample #3 in the pulsed regime in the temperature range (200 – 290) K.

The temperature dependences of resistivity of the samples in the alternate (AC) current regime demonstrate certain well-pronounced features compared to the DC regime. Shown in **Fig. 8** are resistivity vs temperature dependences for all four samples at frequencies 100 Hz, 1, 10 and 100 kHz and the DC curves for comparison. It is seen that all the dependences measured in the AC regime reveal the strong resistivity of activation kind vs. temperature dependences in the higher temperature range, which approach the DC curves at the lowest frequency. Unlike the DC regime, these dependencies tend to saturate for the lower temperatures.

The second very interesting and important feature is revealed for the three samples #1, 2 and 4 with higher resistivity. The resistivity of the samples demonstrates two pronounced activation regimes

in the higher temperature interval and a wave-like transition (with a region of a negative temperature slope) between them. This feature becomes less pronounced and eventually disappears for the sample #3 with lower resistivity. Such a feature can give grounds to suppose the existence of two phases with their own temperature dependences of resistivity in the AC regime in the studied samples. It is also evident that the phases volume ratio changes with the temperature change. The transition between the phases shifts to a higher temperature with the frequency increase. The transition temperature of resistivity and its frequency shift correspond to the temperature of the $tg\delta$ maxima (compare the temperatures of $tg\delta$ maxima in **Fig. 5** with the temperature ranges of wave-like features in **Fig. 8**, and with the temperatures of resistivity maxima in **Fig. C1**).

Also, we should notice that the AC temperature dependences of resistivity have certain correlations with the temperature behavior of the dielectric permittivity (compare the temperature range of wave-like features in **Fig. 8** with the temperature of the dielectric permittivity sharp changes in **Fig. 4**). With lowering temperature, the dielectric permittivity decreases and the resistivity increases. This can evidence the decrease of active polarons concentration participating in the AC conductivity. At the same time, the frequency increase causes a decrease of the dielectric permittivity and resistivity. Also, one may notice the strong non-homogeneity of “carbon doping” of the sintered pellet, which follows from the presented above results and its influence on the DC and AC electric transport characteristics for the samples cut out from different parts of the SPS ceramic pellet.

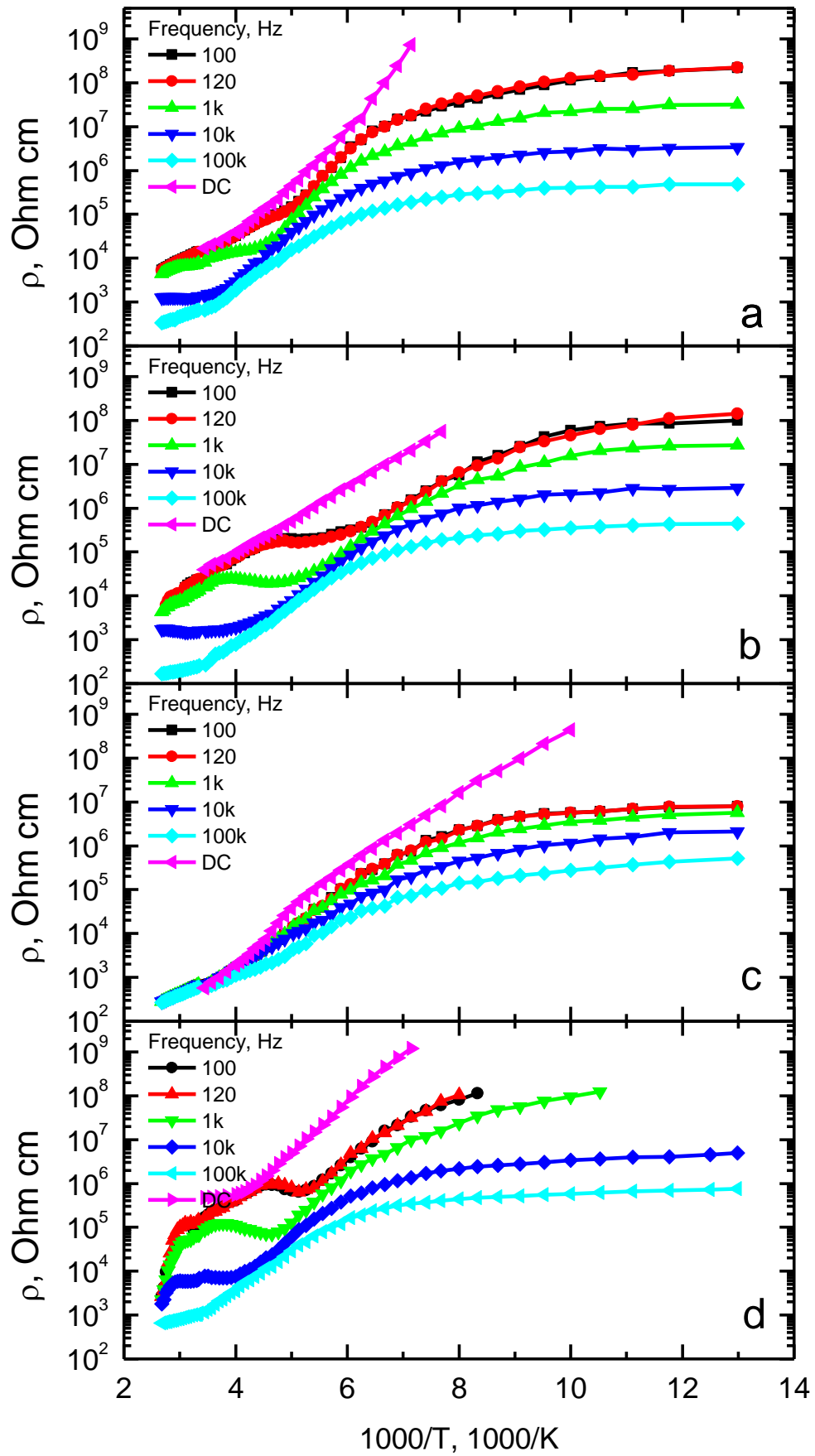


FIGURE 8. The temperature dependences of the samples # 1, 2, 3 and 4 resistivity measured in the AC regime (panels **a**, **b**, **c** and **d**, respectively). Violet DC curves are shown for comparison.

D. Pyroelectric Response Measurements

To clarify the polar state of the BTO ceramics samples obtained by the SPS method, their pyroelectric response has been studied. For pyroelectric studies, the photo-thermo-modulation pyroelectric method [18, 19] was used. In the method, the temperature of the sample changes as $T(t) = T_0 + \Delta T \sin(2\pi f_m t)$ under the influence of a sinusoidally modulated IR radiation flux with intensity $W(t) = \Delta W(1 + \sin 2\pi f_m t)$, where $\Delta T \ll T_0$ and f_m is the modulation frequency. The measured value is the pyroelectric response U_π , caused by the temperature change of the spontaneous polarization $P_s(T)$ of the polar active material. The value of U_π is proportional to the value of the pyroelectric coefficient $\gamma = dP_s(T)/dT$ [20].

The dynamic thermal excitation allows to analyze the amplitude-frequency, $U_\pi(f_m)$, and phase-frequency, $\varphi_\pi(f_m)$, dependences of U_π in a wide frequency range. Under such conditions, it is possible to measure U_π in the pyroelectric current mode, $U_\pi = U_{\pi 1}$, if $2\pi f_m R_L C_s \ll 1$ and in the pyroelectric voltage mode, $U_\pi = U_{\pi 2}$, if $2\pi f_m R_L C_s \gg 1$ (here R_L is the electrical resistance of the load in the circuit of the sensitive element, C_s is the electrical capacitance of the element) [21].

In the case of a uniform distribution of pyroactivity over the thickness, $U_{\pi 1,2}$ depends on the pyroelectric coefficient γ , volume heat capacity C_p and dielectric constant ε of the material and its thickness d [21]. In the pyroelectric current mode, $U_{\pi 1} \propto (\gamma/C_p)R_L/d = \text{const}(f_m)$ and $\varphi_\pi = \varphi_{\pi 1} = \text{const}(f_m)$. Due to the resistive nature of the load in the sample circuit, $U_{\pi 1}(t)$ can be in-phase ($\varphi_{\pi 1} = 0$) or in anti-phase ($\varphi_{\pi 1} = 180^\circ$) with the IR flux intensity $W(t)$, depending on the direction of polarization in the sample. In the pyroelectric voltage mode, $U_{\pi 2} \propto (\gamma/C_p \varepsilon)/f_m$, and $\varphi_\pi = \varphi_{\pi 2} = \text{const}(f_m)$. As a result of the capacitive nature of the load in the sample circuit, there is a phase shift of $\pm\pi/2$ (90° or 270°) between the $U_{\pi 2}(t)$ and the $W(t)$, depending on the polarization direction in the sample. It should be noted that the $U_{\pi 1}$ mode, chosen for the corresponding f_m and R_L so that $2\pi f_m R_L C_s < 1$, transforms into the $U_{\pi 2}$ mode when $2\pi f_m R_L C_s > 1$, and the transition frequency f_{mt} is determined from the relation $2\pi f_{mt} R_L C_s = 1$.

Due to the relationship of the thermal diffusion length $\lambda_T = (a_T/\pi f_m)^{1/2}$ (a_T is the thermal diffusivity) with f_m , it is possible to determine the features of the subsurface distribution of pyroelectric parameters using thermal wave profiling [19]. Since any deviation from a uniform polarization distribution is reflected in the frequency dependences $U_{\pi 1,2}(f_m)$ and $\varphi_{\pi 1,2}(f_m)$, the corresponding λ_T -profiles of pyroelectric response $U_{\pi 1,2}(\lambda_T)$ and phase $\varphi_{\pi 1,2}(\lambda_T)$ can be obtained and analyzed [19].

The results for the SPS BTO ceramics obtained at room temperature are presented in **Fig. 9**. The upper panels show the $U_\pi(f_m)$ dependences, and the lower panels show the dependences of the phase shift $\varphi_\pi(f_m)$ between $U_\pi(t)$ and $W(t)$ for two sides of the BTO sample.

At low frequencies, the U_π value of one side is significantly higher than the other. As f_m increases the values of $U_\pi(f_m)$ of both sides decrease in a different way. At higher frequencies, the values of U_π are almost the same, but corresponding values of $f_m - 1000$ Hz for one side and 200 Hz for other, – are different (see left and right upper panels of **Fig. 9**). For both sides at low frequencies, the values of φ_π are close to 180° , which corresponds to the pyroelectric current mode, but there is no $U_\pi(f_m) = U_{\pi 1} = \text{const}(f_m)$, characteristic of this mode (see above). At higher frequencies, $U_\pi(f_m)$ decreases with increasing f_m , but there is no dependence $U_\pi(f_m) = U_{\pi 2} \sim 1/f_m$, characteristic of the pyroelectric voltage mode. For both sides, the phase $\varphi_\pi(f_m)$ increases with increasing f_m almost logarithmically (lower left and right panels of **Fig. 9**). Therefore, the obtained dependences $U_\pi(f_m)$ and $\varphi_\pi(f_m)$ differ from those being characteristic for a homogeneous polar state.

Estimation of the thermal diffusion length $\lambda_T = (a_T/\pi f_m)^{1/2}$ (the upper axis in **Fig. 9**) for diffusivity $a_T \approx 10^{-6}$ m²/s characteristic of BTO ceramics [22], frequencies $f_m = 10$ Hz and 1 kHz gives $\lambda_T \approx 200$ μm and ~ 20 μm , respectively. Therefore, λ_T is big enough to carry out thermal wave probing of the volume at low frequencies (~ 10 Hz), while at high frequencies (~ 1 kHz) λ_T is short and thermal wave probing of the near-surface region is carried out (as shown in **Fig. 9**).

Thus, the increase in $\varphi_\pi(f_m)$ with increasing f_m (**Fig. 9**) starts from $\varphi_\pi \approx 200^\circ$ under conditions of volume probing ($\lambda_T \sim 100$ μm) and continues under conditions of probing the near-surface layer ($\lambda_T \sim 30$ μm).

The obtained thermo-wave λ_T -profiles of pyroelectric response and phase shift of the SPS BTO ceramics sample are presented in the **Fig. 10**. The decrease in $U_\pi(\lambda_T)$ and increase in $\varphi_\pi(\lambda_T)$ with increase in λ_T (**Fig. 10**) begin under the conditions of volume probing ($\lambda_T \sim 100$ μm) and continue under the conditions of probing the near-surface layer ($\lambda_T \sim 30$ μm). The maximal drop of $U_\pi(\lambda_T)$ begins after transition from the volume to the near-surface probing and correlates with the maximal rise of $\varphi_\pi(\lambda_T)$. It should be also here noted that such decrease of $U_\pi(\lambda_T)$ and increase in $\varphi_\pi(\lambda_T)$ may be associated with the existence not only of polar, but also thermal inhomogeneities, which are caused by graphite inclusions during the ceramic's formation by the SPS method. The specifics of observed λ_T -profiles can be associated with a lower concentration of graphite inclusions in the volume than in the under-surface layer of the BTO ceramics.

Such λ_T -profiles of U_π and φ_π for both sides of the sample corresponds to opposite directions of polarization under both surfaces and, therefore, the existence of an inhomogeneous counter-polarized state, like those observed for TGS-PEO composites [19].

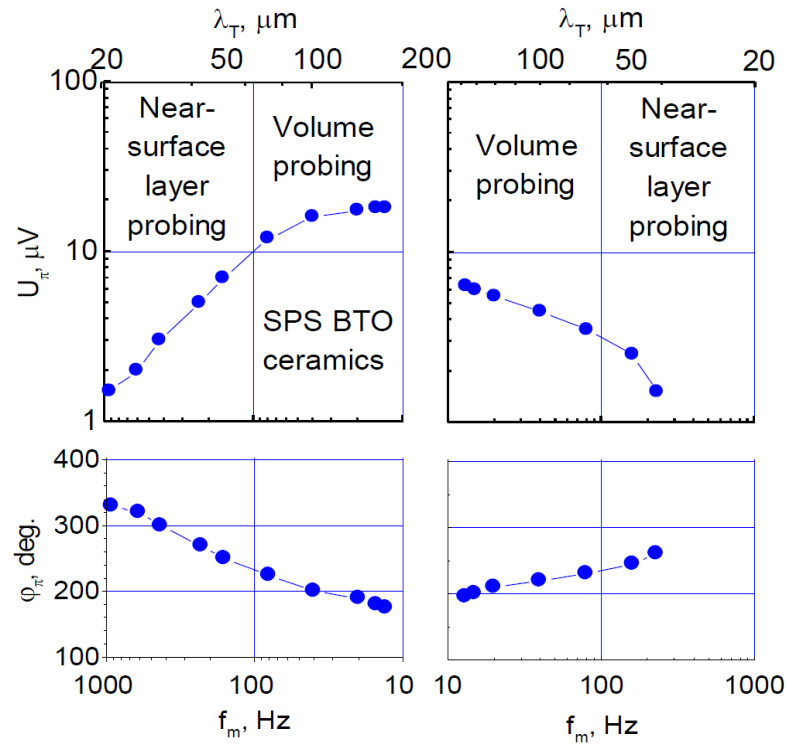


FIGURE 9. Dependences of the pyroelectric response amplitude (upper panels) and its phase shift (lower panels) of the SPS BTO ceramics vs. the modulation frequency of the thermal flux.

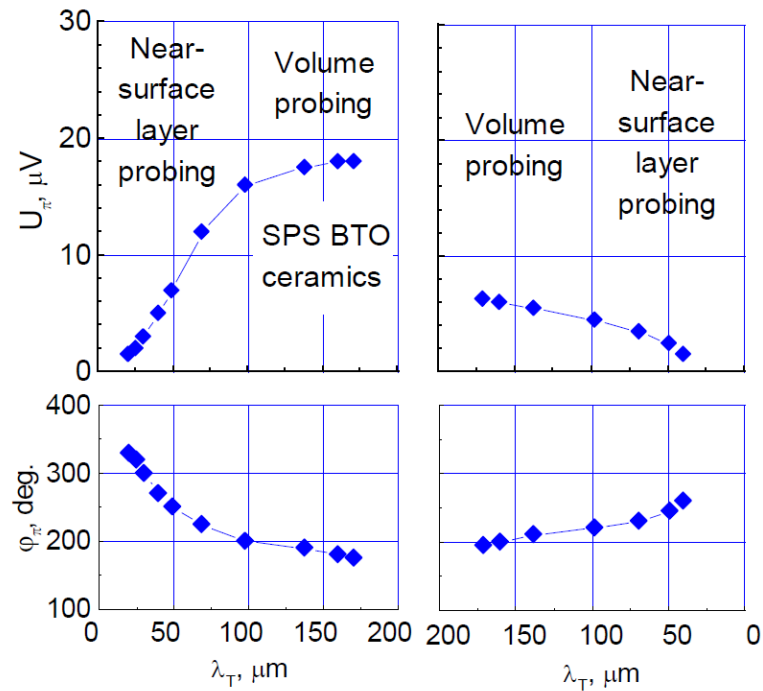


FIGURE 10. Thermo-wave profiles of the pyroelectric response amplitude (upper panels) and phase shift (lower panels) of the SPS BTO ceramics.

E. Theoretical Analysis of the Dielectric Response

E1. The Dielectric Response of the HPS ceramic. At relatively low temperatures, which are well below the ferroelectric-paraelectric transition temperature T_{FE} of the BTO ceramics, a significant volume fraction of the ceramics is in the polarized ferroelectric phase. Since the size of the used BTO nanoparticles is small and changes from 17 nm to 47 nm, the ferroelectric-paraelectric transition can be strongly diffused due to the dispersion of the grain sizes in ceramics. Even well below T_{FE} the grains, which sizes are smaller the critical size, are paraelectric; the bigger grains can be ferroelectric with a very low spontaneous polarization, and only the biggest grains can have a spontaneous polarization close to the bulk BTO single crystal. To minimize to the strong depolarization electric fields created by the spontaneous polarization of the grains, the polarized grains acquire the core-shell structure: the polarized core is ferroelectric and insulating, and the “screening” shell is paraelectric and semiconducting (i.e., contains the free charge carriers). The core-shell structure of BTO grains is shown in **Fig. 11(a)**. Here the spontaneous polarization of the biggest grain cores is shown by colored arrows, and the screening paraelectric shells are shown by thin colored layers around the cores. At $T \ll T_{FE}$ the carriers appear “trapped” by the polarized grains. The carriers should gradually “release” under the temperature increase for all those grains, which spontaneous polarization decreases and eventually disappears once the grains become paraelectric (and therefore non-polarized) at $T \gg T_{FE}$ (see **Fig. 11(b)**).

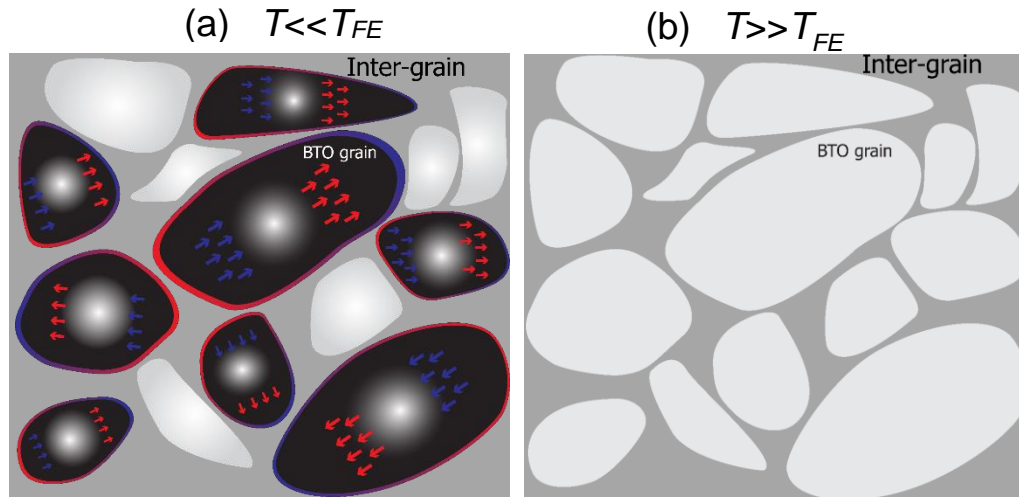


FIGURE 11. Schematic illustration of the paraelectric (light-grey color) and ferroelectric (dark-grey colors) grains, and inter-grain space (grey color) inside the HPS ceramics for $T \ll T_{FE}$ **(a)** and $T \gg T_{FE}$ **(b)**. The colored arrows show the direction and magnitude of the spontaneous polarization inside the ferroelectric grain cores. The colored contours correspond to the semiconducting shells, which contain the screening charges.

In dependence on the temperature, carrier density and mobility, the charge carriers could create the regions with high conductivity between the grains. Due to the release of free carriers in the inter-grain space, the increase of electric current appears near the transition temperature, as well as the pronounced maxima of the current should appear near the coercive field. For the temperatures well above T_{FE} and/or far away from other structural transitions the current and corresponding losses should be minimal, because an “extra” charge drains through the electrodes. This well-known behavior of the inter-grain conductance can explain the temperature dependence of the pyroelectric current in dense HPS ferroelectric ceramics, as well as it predicts the losses maxima near the structural (i.e., rhombohedral-orthorhombic and orthorhombic-tetragonal) and paraelectric-ferroelectric phase transitions observed in the studied HPS BTO ceramics (see e.g., **Fig. 3**).

Note, that the classical Debye relaxation model predicts the maxima of dielectric losses and double maxima separated by the minima of the dielectric permittivity real part near T_{FE} (see e.g., Eqs.(1)-(2) in Ref.[23]), which are observed in some ferroelectrics (see e.g. Fig. 1 and 2 ibidem).

E2. The Dielectric Response of the SPS ceramic. Neither the trap-and-release mechanism of the free charges in the shells and/or the inter-grain space, nor the pure Debye relaxation model of dielectric response can explain the electrophysical properties observed for the SPS BTO ceramics. Below we consider several possible mechanisms, which can lead to the giant values of the relative dielectric permittivity ($>10^5$) accompanied by the very high values of dielectric losses ($tg\delta > 1$) in the strongly inhomogeneous ferroelectric-semiconducting SPS ceramics.

The first mechanism is the effect of “geometric” capacitance, which could appear in the highly porous mixtures of the insulating and conducting inclusions. In this case the effective surface area of the capacitor could be much larger than the electrodes area, and the effective area could accumulate the space charge. We verified the geometric capacitance effect contribution by measuring the capacitance of the SPS BTO ceramic samples of different cutting angles, thickness, electrode area, frequency, and temperature, which does not reveal any scaling laws characteristic for the effect. Also, the microscopy observations do not confirm the high porosity of the studied samples. Hence, the geometric capacitance effect can be reliably excluded from the further consideration.

The second mechanism is the Maxwell-Wagner effect [11], which could lead to the apparent enhancement of the dielectric response in the dielectric-semiconducting mixture in the presence of insulating polar grains, screening shells and conductive graphite inclusions. In principle all conductivity effects in the inhomogeneous media are strongly inter-wined and closely related with possible electric percolation effects. To consider the possible role and relative contributions of the conductivity effects a few theoretical models are considered below.

According to the effective media model proposed by Liu et al. [12], the one can consider two (or more) layers representing all grain cores, their screening shells and grain boundaries, graphite inclusions and inter-grain space in the Maxwell-Wagner approach. One of the “effective” layers has a thickness l and corresponds to weakly-conductive grain cores, and the other has a thickness d and corresponds to all stronger conductive regions (such as screening shells, grain boundaries and/or inter-grain space). The layers are characterized by the effective dielectric permittivity and conductivity: ε_g and σ_g for grain cores, ε_{gb} and σ_{gb} for grain boundaries and/or inter-grains. These effective parameters are temperature and/or frequency dependent. Assuming that the expression for capacitance of the series connection of the layers is valid, $\frac{l+d}{\varepsilon_{eff}} = \frac{l}{\varepsilon_g - i\frac{\sigma_g}{\omega}} + \frac{d}{\varepsilon_{gb} - i\frac{\sigma_{gb}}{\omega}}$, the effective permittivity of the SPS ceramics, ε_{eff} , is a complex function of the temperature T and frequency ω of applied voltage, which can be presented in the form [12]:

$$\varepsilon_{eff}(T, \omega) = (l + d) \left(\frac{l}{\varepsilon_g - i\frac{\sigma_g}{\omega}} + \frac{d}{\varepsilon_{gb} - i\frac{\sigma_{gb}}{\omega}} \right)^{-1} \approx \varepsilon_\infty + \left(\varepsilon_s - \varepsilon_\infty - i \frac{\sigma}{\varepsilon_s \omega} \right) \frac{1}{1 + i\omega\tau}. \quad (1a)$$

Here the following designations are introduced:

$$\varepsilon_\infty = \frac{l+d}{l/\varepsilon_g + d/\varepsilon_{gb}}, \quad \varepsilon_s = \left(\frac{\varepsilon_g}{\sigma_g} + \frac{\varepsilon_{gb}}{\sigma_{gb}} \right) \frac{l+d}{l/\sigma_g + d/\sigma_{gb}}, \quad \tau = \frac{l\varepsilon_{gb} + d\varepsilon_g}{l\sigma_{gb} + d\sigma_g}, \quad \sigma = \frac{l+d}{l/\sigma_g + d/\sigma_{gb}}. \quad (1b)$$

The complex dielectric permittivity in the right-hand side of Eq. (1a) consists of three contributions. The first term, ε_∞ , is the high-frequency limit of the dielectric permittivity determined by the dielectric permittivity of effective layers connected in series, namely $\varepsilon_{eff}(T, \omega \rightarrow \infty) \rightarrow \varepsilon_\infty$. The parameter ε_s is the low-frequency limit of the dielectric permittivity real part, because $\text{Re}[\varepsilon_{eff}(T, \omega \rightarrow 0)] \rightarrow \varepsilon_s$. The value of ε_s is determined by the permittivity-to-conductivity ratios, as well as by the conductivity of the layers connected in series. The parameter σ describes the contribution of the layers' conductivity. The time τ rules the timescale of the Debye-type relaxation determined by the conductivity and permittivity of the effective layers.

In the case when the grain cores are insulating (i.e., $\sigma_g = 0$), the pure Debye relaxation occurs and $\varepsilon_{eff}(T, \omega) \approx \varepsilon_\infty + (\varepsilon_s - \varepsilon_\infty) \frac{1}{1 + i\omega\tau}$, where $\varepsilon_s = \varepsilon_g \left(1 + \frac{d}{l} \right)$ and $\tau = \frac{\varepsilon_{gb}}{\sigma_{gb}} + \frac{d\varepsilon_g}{l\sigma_{gb}}$. Thus, the strong increase of the low-frequency permittivity ($\varepsilon_s \gg \varepsilon_g$) is possible for $d \gg l$, i.e. the volume fraction of the screening shells, grain boundaries and inter-grain space are much larger than the fraction of grain cores. Since $\varepsilon_\infty \equiv \varepsilon_g \left(1 + \frac{d(\varepsilon_{gb} - \varepsilon_g)}{\varepsilon_{gb}l + \varepsilon_g d} \right)$, the significant increase of the high-frequency permittivity ($\varepsilon_\infty \gg \varepsilon_g$) is possible only when $\varepsilon_{gb} \gg \varepsilon_g$ and $d \gg l$ simultaneously. As it should be $\varepsilon_\infty < \varepsilon_s$, independently on the conductivity of the effective layers.

In the case when the morphology of the grains' connection is very complex, and the simplest model of series connection is not applicable, in **Appendix B** we derived the following expression for the effective permittivity:

$$\varepsilon_{eff}^*(T, \omega) \approx \varepsilon_{gb}^* \left[1 + \frac{\mu(\varepsilon_g^* - \varepsilon_{gb}^*)}{n_g \varepsilon_g^* + (1 - n_g) \varepsilon_{gb}^* - n_g \mu (\varepsilon_g^* - \varepsilon_{gb}^*)} \right], \quad (2)$$

where the parameter μ has the meaning of the relative volume fraction of grains and n_g is the depolarization factor of the grains in the direction of applied electric field, which assumed to have an ellipsoidal shape and uniformly oriented.

It is seen that expression (2) gives $\varepsilon_{eff}^* = \varepsilon_{gb}^*$ and $\varepsilon_{eff}^* = \varepsilon_g^*$ for $\mu = 0$ and $\mu = 1$ respectively, as it should be expected. For the system consisting of the layers, perpendicular to the electrodes (i.e., for $n_g = 1$) Eq.(2) gives the analog of Eq.(1a), $\varepsilon_{eff}^* = \left(\frac{1-\mu}{\varepsilon_{gb}^*} + \frac{\mu}{\varepsilon_g^*} \right)^{-1}$. For the system consisting of the spherical grains (i.e., for $n_g = 1/3$) Eq.(2) gives the Wagner formulae, $\varepsilon_{eff}^* = \varepsilon_{gb}^* \left[1 + \frac{3\mu(\varepsilon_g^* - \varepsilon_{gb}^*)}{\varepsilon_g^* + 2\varepsilon_{gb}^* - \mu(\varepsilon_g^* - \varepsilon_{gb}^*)} \right]$. For the system of the columns, parallel to the electrodes, i.e., for $n_g = 0$, Eq.(2) gives the expression $\varepsilon_{eff}^* = (1 - \mu)\varepsilon_{gb}^* + \mu\varepsilon_g^*$, which is the equivalent to the system with paralleled capacitors.

Since the X-ray diffraction and NMR studies confirm the coexistence of the tetragonal ferroelectric and cubic paraelectric phases in the (15 – 45)-nm BTO nanopowders [24, 25] used for the preparation of the SPS ceramics, it is very likely that the temperature behavior of its dielectric permittivity ε_g is close to those of HPS ceramics, shown in **Fig. 3** (i.e., has a pronounced Curie-Weiss behavior near the paraelectric-ferroelectric transition at about 125°C). Therefore, a rather general approximation functions for ε_g^* can be used:

$$\varepsilon_g^*(r, \omega, T) = \frac{C_{CW}}{\sqrt{(T - T_g(r, \omega))^2 + \Delta(\omega)^2}} - i \frac{\sigma_g}{\omega}, \quad (3a)$$

$$T_g(r, \omega) = T_{CB} \left(1 - \frac{A_1}{r} - \frac{A_2(\omega)}{r^2} - \dots \right), \quad (3b)$$

In Eq.(3a) r is the grain core radius, C_{CW} and $\Delta(\omega)$ are the effective Curie-Weiss constant and the frequency-dependent dispersion of the dielectric permittivity maximum, respectively. As a rule, $\Delta(\omega)$ increases with the frequency increase and the dependence is especially strong for the relaxor-like ferroelectrics. In Eq.(3b), T_{CB} is the Curie temperature of a bulk BTO single crystal. The parameters A_i ($i = 1, 2$) originated from the strain-electrostriction coupling, intrinsic stresses (such as surface tension) and dipole-dipole correlation effects coupled with electrostriction, respectively [26, 27]. The parameter $A_1 \sim \mu(Q_{11} + 2Q_{12})$ is positive for the quasi-spherical BaTiO₃ nanoparticles, because the

surface tension coefficient μ is positive for the thermodynamically stable surface and corresponding combination of electrostriction coefficients, $Q_{11} + 2Q_{12}$, are positive too [26, 27]. The parameter $A_2 \sim \frac{g}{\lambda}$ is small and positive for the dipole-dipole correlations inside the single-domain ferroelectric nanoparticle [26], because the corresponding combination of polarization gradient coefficients g and extrapolation length λ are positive in the case. As a rule, higher coefficients A_i ($i > 2$) are positive and negligibly small. The dielectric permittivity of the grain calculated using Eq.(3) allowing for the averaging over the grain radius (e.g., from 5 nm to 50 nm, the average size is 25 nm) is shown in **Fig. 12(c)**. The curves in the figure reproduce the main features of the dielectric response for HPS ceramics observed in the wide frequency range 100 Hz – 100 kHz (compare **Fig. 12(c)** with **Fig. 3**). Note that ε_g reaches high values $\sim(2 - 3) \cdot 10^3$ only in the vicinity of T_{FE} , and is significantly lower than 10^3 for other temperatures.

Since the dielectric permittivity of the studied SPS BTO ceramics is very high ($>10^5$) even at relatively high frequencies ($\omega \geq 100$ kHz) and has a plateau-like form in the broad temperature range (from -50°C to 200°C), the anomalous temperature dependence could originate only from the “giant” dielectric permittivity of superparaelectric shells, grain boundaries and/or inter-grain regions. Thus, we should regard that $\varepsilon_{gb} \gg \varepsilon_g$ and may assume that the shells and inter-grain regions can exhibit polaronic properties too.

In the polaronic model [12], individual polarons can be divided into two groups with different thermal activation behavior. Using the model [12], we assume that the first group of the polarons requires a thermal activation to overcome a local energy barrier before they can contribute to the inter-grain conductivity σ_{gb} and giant permittivity $\varepsilon_{gb} \gg \varepsilon_g$. For sufficiently low temperatures most of the polarons charge are “trapped” around their equilibrium positions, and their contribution to the conductivity and permittivity is a small constant. As the temperature increases, the fraction of polarons, which can jump from one energy minimum to others being still bounded by the grain boundaries, increases. In result, the polaronic contribution to the effective dielectric response increases. Using the statistical model for relaxors evolved by Liu et al [28], one can estimate the relative fractions of active (f) and inactive ($1 - f$) polarons from the Maxwell-Boltzmann distribution as [12]:

$$f(E_b, T) = \sqrt{\frac{4E_b}{\pi k_B T}} \exp\left(-\frac{E_b}{k_B T}\right) + \text{Erfc}\left[\sqrt{\frac{E_b}{k_B T}}\right]. \quad (4a)$$

Here E_b is the average depth of the polaron potential well, k_B is the Boltzmann constant, T is the absolute temperature (in Kelvin), and Erfc is the complementary error function. The fraction of active polarons is negligibly small at $k_B T \ll E_b$, monotonically increases with the temperature increase and tends to 1 for $k_B T \gg E_b$. The function (4a) is shown by the dashed curve in **Fig. 12(b)**.

For better agreement with the observed temperature dependences of the dielectric response and losses, instead of Eq.(4a) we selected the smooth step-like function for $f(E_b, T)$:

$$f(E_b, T, \omega) = \frac{1}{2} \left(1 + \text{Tanh} \left[\frac{k_B}{E_b(\omega)} (T - T_a(\omega)) \right] \right). \quad (4b)$$

Here T_a has the meaning of the polarons activation temperature and E_b regulates the steepness of the step-like activation function. Below we assume that the polaron activation is a kinetic process, and therefore T_a and E_b can be weakly (e.g., logarithmically) frequency-dependent, and their frequency dependence can be determined from the fitting. The assumption (4b) of the step-like activation of polarons at a definite temperature $T_a(\omega)$ is grounded by the experimentally observed frequency-dependent transition of the electric transport mechanism accompanied by the maxima of losses (see the wave-like features in **Fig. 8**, the maxima of $tg\delta$ in **Fig. 5** and the resistivity maxima in **Fig. C1**). The function (4b) is shown by the solid curve in **Fig. 12(b)**, where the values of T_a and E_b were selected from the best agreement of the polaron model with the dielectric response shown in **Figs. 4 – 5**.

Below we assume that the effective dielectric permittivity of the inter-grain space is given by expression:

$$\varepsilon_{gb}^*(T, \omega) = f(E_b, T)\varepsilon_{SP}(T, \omega) + [1 - f(E_b, T)]\varepsilon_b - i\frac{\sigma_{gb}}{\omega^\alpha}. \quad (5)$$

Here $\varepsilon_{SP}(T, \omega)$ and ε_b are the dielectric permittivity from the active and inactive polaron groups, respectively. Let us assume that $\varepsilon_{SP}(T, \omega) \gg \varepsilon_b$ and regard that ε_b is temperature- and frequency-independent, while the superparaelectric-like contribution, $\varepsilon_{SP}(T, \omega) \cong \frac{C_{SP}}{\sqrt{(T-T_{SP}(r, \omega))^2 + \Delta_{SP}(\omega)^2}} + \varepsilon_b$,

is regarded dependent on these parameters. The fitting parameter α can vary from -1 (for conducting elements connected in series) to +1 (for parallel connection of the conducting elements). The range $-1 < \alpha < 1$ corresponds to the mixed-type connection of conducting elements as well as to the non-Debye relaxation in the inter-grain regions. Note that Eq.(5) is similar to the corresponding expression in Ref. [12] for $\alpha = 1$.

Substitution of expressions (3), (4a) and (5) in Eq.(1), which corresponds to the bilayer Maxwell-Wagner model, leads to the closed-form expression for $\varepsilon_{eff}(T, \omega)$, which temperature dependence can be compared with experiment. Using multiple fitting parameters included in Eq.(1) and (4a), we failed to describe the experimental results shown in **Figs. 4** and **5** even semi-quantitatively. One of the assumptions, which is required for a qualitative description, is the inequality $l/d \leq 0.01$. The inequality is quite unphysical because it means that the volume fraction of ferroelectric grains (l) is at least 100 smaller than the volume fraction (d) of the inter-grain space.

Next we substitute the expressions (3), (4b) and (5) in Eq.(2) and compared the obtained dependence $\varepsilon_{eff}(T, \omega)$ with the experiment. Corresponding theoretical results shown in **Figs. 12(d)**-

(f) are in a qualitative and semi-quantitative agreement with the experimental results shown in **Figs. 4** and **5**.

The dielectric permittivity of the shell and inter-grain regions calculated from Eq.(5) is shown in **Fig. 12(d)**. The curves in the figure illustrate the giant dielectric response of the superparaelectric-like shells and inter-grain regions in the frequency range from 100 Hz to 100 kHz (compare **Fig. 12(d)** with **Figs. 4**). For better comparison with experiment, we regarded that the frequency dependence of $T_{SP}(r, \omega)$ and $\Delta_{SP}(\omega)$ obeys a weak logarithmic law.

The real part of the effective dielectric permittivity $\text{Re}[\varepsilon_{eff}]$ calculated from Eqs.(2), (3), (4b) and (5) is shown in **Fig. 12(e)**. The curves in the figure reproduce semi-quantitatively the main features of the dielectric permittivity of the SPS ceramics observed in the frequency range from 100 Hz to 100 kHz (compare **Fig. 12(e)** with **Fig. 4**). The parameter $\mu = 0.8$, which corresponds to the best fitting of Eq.(5) to experiment, is quite realistic meaning that the volume fraction of ferroelectric grains comprises 80 % and the volume fraction of inter-grain space is 20 %. The depolarization factor, $n_g = 0.33$, corresponds to the “effective” spherical shape of the grains, which is also quite reasonable.

The loss angle tangent, $tg\delta = \text{Im}[\varepsilon_{eff}]/\text{Re}[\varepsilon_{eff}]$, calculated from Eqs.(2), (3), (4b) and (5) is shown in **Fig. 12(f)**. The curves in the figure reproduce qualitatively several main features of the losses observed in the SPS ceramics is in the frequency range from 100 Hz to 100 kHz (compare **Fig. 12(f)** with **Fig. 5**). The parameter α in Eq.(5), determined from the fitting, appears equal to 0.17. This reflects the fact that the dielectric response relaxation is significantly non-Debye in the shells, grain boundaries and inter-grain space, as anticipated for the mixed-type electric connection of the ferroelectric, superparaelectric-like and semiconducting regions. The mixed-type connection of the equivalent conductive elements is corroborated by the frequency behavior of the $tg\delta$ maxima shown in **Fig. 5**.

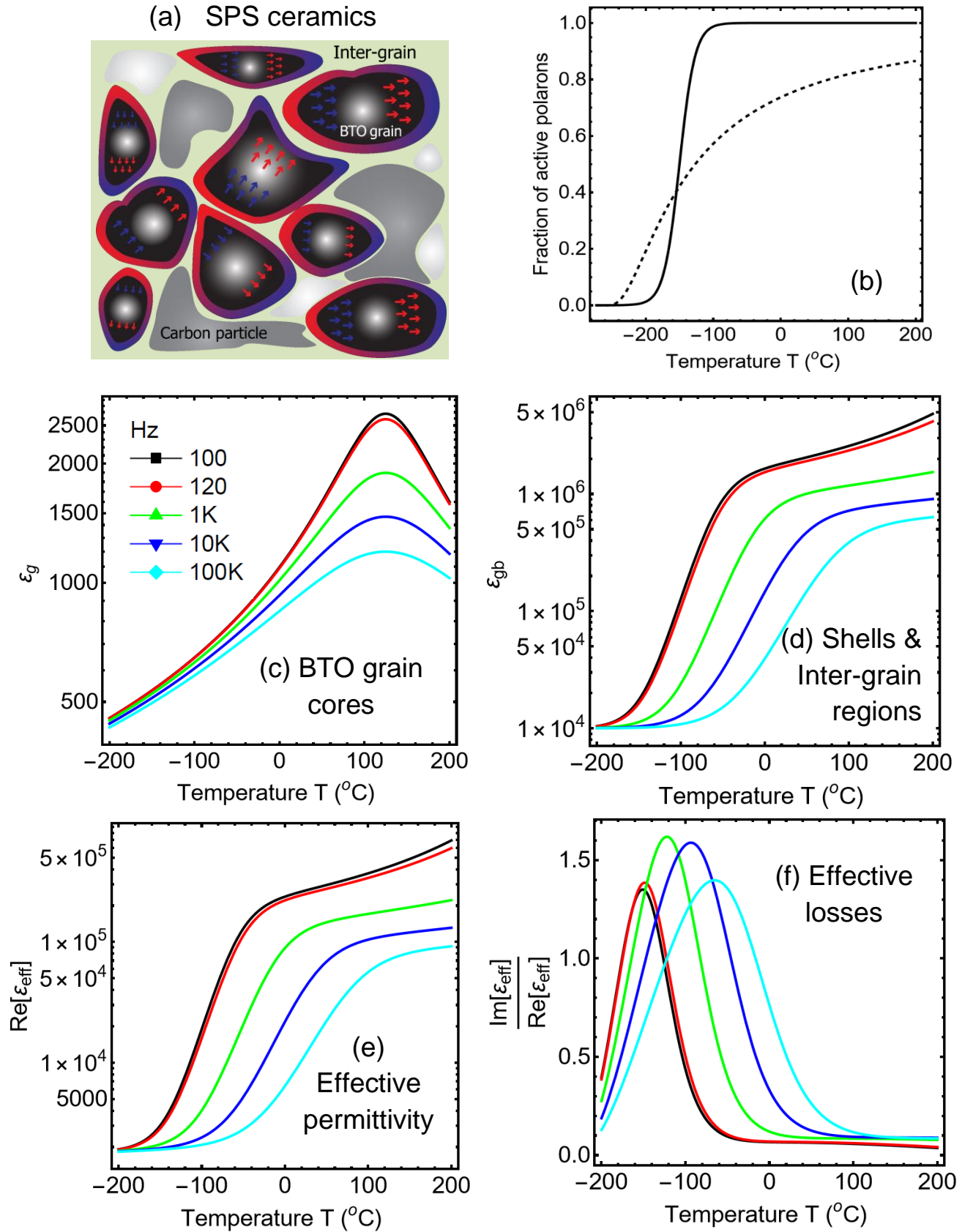


FIGURE 12. (a) Schematic illustration of the paraelectric (light-grey color) and ferroelectric (dark-grey colors) grains, inter-grain space (light-olive color) and graphite inclusions (dark-grey color) inside the SPS ceramics for $T \ll T_{FE}$. The colored arrows show the direction and magnitude of the spontaneous polarization inside the ferroelectric grain cores. The colored contours correspond to the semiconducting shells, which

contain the screening charges. **(b)** The fraction of active polarons calculated from Eq.(4b) for $T_a = -150^\circ\text{C}$ and $E_b = -250^\circ\text{C}$ (solid curve) and from Eq.(4a) for $E_b = -100^\circ\text{C}$ (dashed curve). **(c)** The dielectric permittivity of the grain calculated using Eq.(3) allowing for the averaging over the grain radius for BTO parameters $C_{CW} = 1.5 \cdot 10^6$ K, $T_{CB} = 398$ K, $\Delta(\omega) = 20 + 20 \log\left(\frac{\omega}{\text{Hz}}\right)$, $A_1 \cong 5$ nm and $A_2 < 0.5$ nm². **(d)** The dielectric permittivity of shell and inter-grain regions calculated from Eq.(5) for $\varepsilon_R \cong 10^6$ and $\varepsilon_b = 10^4$. The real part of the effective dielectric permittivity **(e)** and loss angle tangent **(f)** of SPS ceramics calculated from Eqs.(2)-(5) for $\mu = 0.8$, $n_g = 0.33$ and $\alpha = 0.17$. The curves in the panels **(c)-(f)** correspond to the frequencies $\omega = 100$ Hz (black curves), 120 Hz (red curves), 1 kHz (green curves), 10 kHz (blue curves) and 100 kHz (cyan curves).

The fitting functions for the grain and inter-grain conductivity, $\sigma_g = 7 \cdot 10^3 \exp\left[-\frac{500}{T}\right]$ 1/s and $\sigma_{gb} = 7 \cdot 10^5 \exp\left[-\frac{300}{T}\right]$ 1/s, obey the activation Arrhenius law. The inequality $\sigma_g \ll \sigma_{gb}$ well agrees with our assumption that graphite inclusions inject carriers in the inter-grain space. Moreover, for the definite concentration of the graphite inclusions the apparent superparaelectricity appears. The percolation cluster appears under the temperature increase due to the release of free carriers in the inter-grain space and drastically increases the conductivity (as shown in **Fig. 5(c)**).

III. DISCUSSION AND CONCLUSIONS

We revealed the anomalous temperature behavior of the complex dielectric permittivity and unusual frequency dependences of the pyroelectric response of the fine-grained ceramics prepared by the SPS of the ferroelectric BTO nanoparticles with the average size 25 nm.

Unexpectedly, the real part of the relative dielectric permittivity sharply increases from 10^3 to 10^5 with the temperature rise from -150°C to -50°C ; then it quickly saturates to giant values ($\sim 5 \cdot 10^5$) and remains on the quasi-plateau in the broad temperature range ($20 - 200$) $^\circ\text{C}$. The dielectric losses are very high ($tg\delta \sim 0.3 - 3$) and have a pronounced maxima in the region of the steep increase of the dielectric permittivity, which height increases slightly and position shifts strongly to the higher temperatures with the frequency increase. The temperature dependences of the electro-resistivity indicate the frequency-dependent transition in the electro-transport mechanisms between the lower and higher conductivity states accompanied by the maximum in the temperature dependence of the $tg\delta$.

The above-mentioned anomalous behavior of the dielectric response and losses of the SPS ceramic, which is observed in a broad frequency range (0.1 – 100) kHz, does not reveal any features of the ferroelectric-paraelectric phase transition near 125°C (as for the single-crystalline BTO) or at lower temperatures (as for the small BTO nanoparticles). The observed behavior is principally different from the typical behavior of the dielectric response of the HPS ceramics prepared from the

same BTO nanoparticle powders, where we observed a pronounced maximum of the dielectric permittivity near 125°C corresponding to the ferroelectric-paraelectric phase transition. At the same time, the pyroelectric thermal probing at the opposite surfaces of the SPS ceramic samples reveals the existence of the spatially inhomogeneous counter-polarized ferroelectric state. The state can be induced by thermal and/or conductive inhomogeneities. According to the SEM and Raman spectroscopy data, the inhomogeneities are graphite inclusions, which are non-uniformly distributed in the SPS ceramics.

Since the pyroelectric response proves the presence of the spontaneously counter-polarized regions in the SPS ceramics, and since the dielectric measurements reveal the giant permittivity and high losses characteristic for the superparaelectric-like and semiconducting states, we assumed that the ceramics can be imagined as a strongly inhomogeneous media with electrically coupled weakly conductive ferroelectric regions, semiconducting superparaelectric-like regions and conducting graphite regions.

From the theoretical standpoint, the complex dielectric response of such inhomogeneous media can be described in the framework of effective media approach allowing for the Maxwell-Wagner effect. Using the core-shell model for ceramic grains and inter-grain space we reached the qualitative and semi-quantitative description of the observed anomalous temperature behavior of the giant dielectric response. Within the model the grain cores are regarded ferroelectric and weakly conductive, and their shells, the inter-grain space and grain boundaries are regarded semiconducting due to the high concentration of space charges in the presence of graphite inclusions. The superparaelectric-like state with giant dielectric response can appear in the semiconducting shells, inter-grain spaces and grain boundaries due to the step-like thermal activation of localized polarons at a definite temperature. The assumption of the polaron activation is grounded by the experimentally observed frequency-dependent phase transition of the electro-transport mechanism accompanied by the maximum of losses.

Obtained experimental results and evolved models for the description of anomalous temperature behavior of the giant dielectric response and losses can be the key for the description of complex electrophysical properties inherent to the strongly inhomogeneous media with electrically coupled insulating ferroelectric nanoregions and semiconducting superparaelectric-like regions.

Acknowledgments. The samples preparation, characterization and results analysis are sponsored by the NATO Science for Peace and Security Programme under grant SPS G5980 “FRAPCOM” (O.S.P, S.I., and A.N.M.). Electrophysical measurements are sponsored by the Target Program of the National Academy of Sciences of Ukraine, Project No. 4.8/23-p (O.S.P., N.V.M., V.N.P., and V.V.V). Theoretical calculations performed by A.N.M. are funded by EOARD project 9IOE063b and related

STCU partner project P751b. Analytical results, presented in this work, are visualized in Mathematica 14.2 [29].

Author contributions. O.S.P. conceived, performed (jointly with M.Y.Y., D.O.S. and O.V.B.) and analyzed results of the dielectric and electrophysical experiments. S.E.I., B.P. and V.K. prepared the SPS ceramics and wrote Appendix A. A.S.N. performed Raman studies. V.I.S. performed the SEM measurements and wrote Appendix B. O.V.L. prepared the HPS ceramics. N.V.M. performed the pyroelectric measurements (jointly with M.Y.Y.) and analyzed results. A.N.M. and E.A.E. proposed analytical models of the dielectric response and interpreted theoretical results. The research idea, manuscript writing, and improvement belong to the corresponding authors, N.V.M., V.V.V. and A.N.M.

APPENDIX A. Samples characterization

A1. Samples characterization by the Scanning Electron Microscopy (SEM)

The BTO ceramics were studied in the JSM-35 scanning electron microscope. Two detectors of different types were used to obtain the image. They are the detector of slow secondary electrons and the detector of backscattered fast electrons. For the slow-electron detector, the brightness of the image is mainly determined by the topography of the sample (SEI contrast), while for the fast-electron detector, it is determined by the average atomic number Z of the area of the sample irradiated by electrons (Z contrast). However, for both detectors, the second component of the signal is also affected. By comparing these images, it was determined which feature of the sample relates to carbon. This is due to the large difference between the average atomic numbers of ceramics and carbon. For BTO, Z is 33.9, and for carbon it is 6. Therefore, graphite inclusions in the Z contrast mode look significantly darker. But other details of the relief, for example, holes or large pits, can also look dark. That is why the comparison of images was carried out. For example, the images below of one area were obtained using these two detectors. Graphite inclusions are marked by arrows on them. These images show that towards the middle of the sample, the number of carbon inclusions has decreased by about a factor of two.

At the same time, such studies are influenced by the operator's choice of the location of the image acquisition. Therefore, more comprehensive studies were additionally conducted. To do this, images in Z contrast of approximately half of the sample from the edge to its middle were obtained at a small magnification. After processing such an image, it was determined how the contrast Z signal changes from the edge to the middle of the sample. At the same time, a signal from twenty adjacent image lines was taken for averaging. The following figures show such an image and signal. When examining the sample, images of the areas were obtained with a step of 1 mm, starting from the very edge to its middle. These images obtained in Z contrast mode are presented in **Fig. A1**. It can be seen from the signal curve in **Fig. A2** that it increases from the edge of the sample to its middle, which corresponds to a decrease in the number of graphite inclusions in the ceramic.

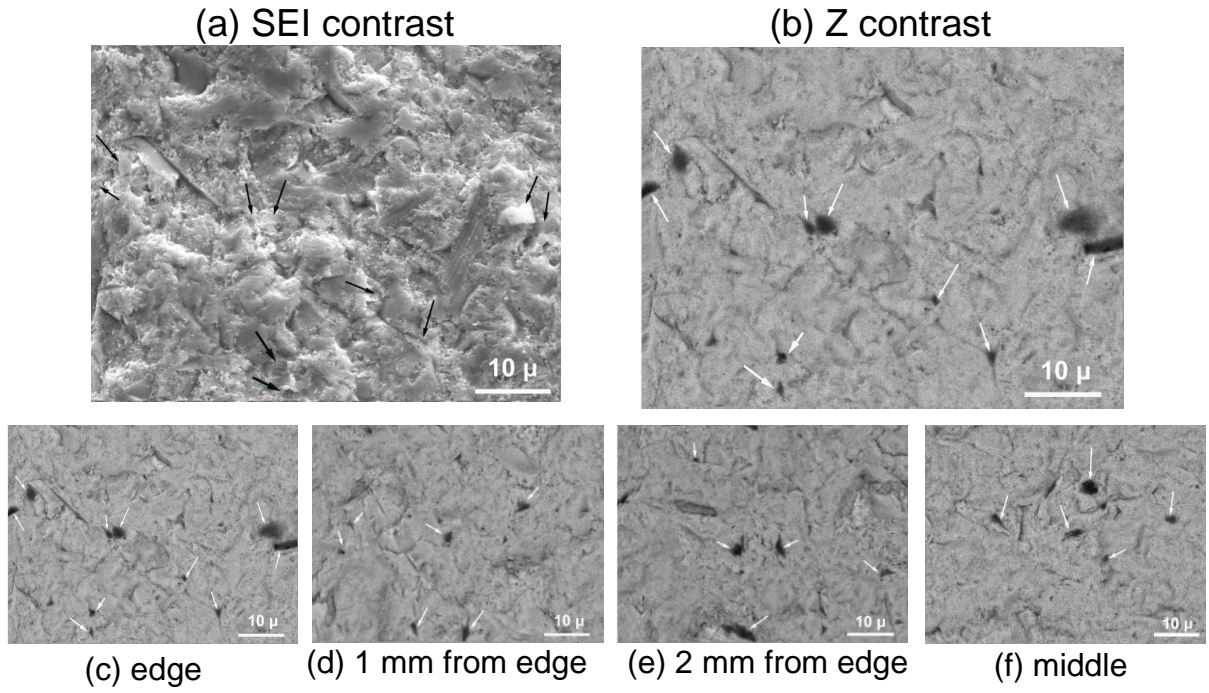


FIGURE A1. (a) SEI contrast and (b) Z-contrast images. Z-contrast images at the pellet edge (c), 1 mm from the edge (d), 2 mm from the edge (e) and in the middle of the pellet (f). White arrows point on the black graphite inclusions.

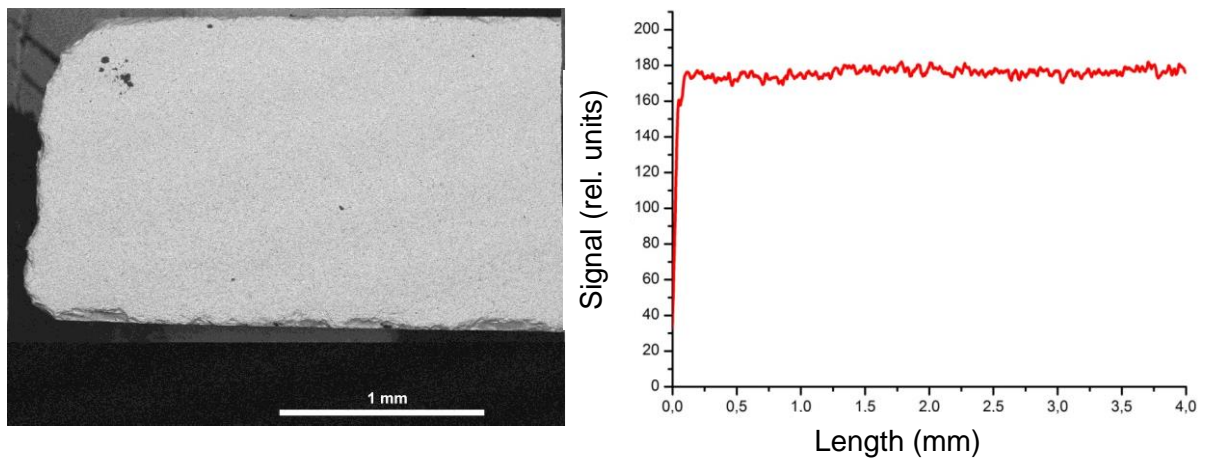


FIGURE A3. The SEM image of the sintered pellet (a) and the signal curve (b).

FIGURE A2. The SEM image of the sintered pellet (a) and the signal curve (b).

APPENDIX B. Generalization of Maxwell-Wagner approach for ellipsoidal-like grains

The idea is based on the exact solution of the problem of ellipsoid with complex dielectric permittivity

$$\varepsilon_g^* = \varepsilon_g - i \frac{\sigma_g}{\omega} \text{ placed in dielectric homogeneous matrix with complex permittivity } \varepsilon_{gb}^* = \varepsilon_{gb} - i \frac{\sigma_{gb}}{\omega}.$$

The external electric field E_{ext} has a fixed value far from the ellipsoid. It is well-known (see e.g., Ref.[30]) that the field inside the ellipsoid is homogeneous and equal to

$$E_g = \frac{\varepsilon_{gb}^*}{n_g \varepsilon_g^* + (1-n_g) \varepsilon_{gb}^*} E_{ext}. \quad (\text{B.1})$$

Here we supposed that the external electric field is pointed along one of the ellipsoid principal axes, for which the depolarization factor is n_g . The excess dipole moment p_g of the ellipsoidal grain with semiaxes a , b and c is equal to:

$$p_g = \varepsilon_0 \frac{4\pi}{3} abc \frac{\varepsilon_g^* - \varepsilon_{gb}^*}{n_g \varepsilon_g^* + (1-n_g) \varepsilon_{gb}^*} E_{ext}. \quad (\text{B.2a})$$

Below we use the approach proposed by Wagner [31] to derive the effective dielectric permittivity for the system of uniformly oriented dielectric ellipsoids of the same shape, separated far enough to neglect their mutual dipole-dipole interaction. Below we suppose that all grains are oriented along the external electric field, as well as the total dipole moment $m p_g$ of all the ellipsoidal grains should be equivalent to the total dipole moment of the virtual volume, which has the same shape and is filled with the matter of the effective permittivity ε_{eff}^* . An observer, who is unaware of the presence of the elliptical grains and who makes measurements on the substance, would find this apparent dielectric permittivity.

Let us calculate ε_{eff}^* using the following consideration. Imagine a “big” ellipsoid with semiaxes A , B and C , which contain a number m of small ellipsoidal grains of the same shape. The space outside the “big” ellipsoid should contain the substance with permittivity ε_{gb}^* . In this space, therefore, at a sufficiently large distance from the “big” ellipsoid, the electrostatic potential is determined by the two contributions, namely those of the homogeneous field and the contribution of all the m dipoles with the moments given by (B.2a), so that the total dipole moment is $p_{eff} = m \cdot 4\pi abc P_g / 3$. If we now imagine that the virtual “big” ellipsoid with semiaxes A , B and C is filled by the substance with the effective permittivity ε_{eff}^* , the corresponding electric potential is determined by the presence of the dipole moment

$$p_{eff} = \varepsilon_0 \frac{4\pi}{3} ABC \frac{\varepsilon_{eff}^* - \varepsilon_{gb}^*}{n_g \varepsilon_{eff}^* + (1-n_g) \varepsilon_{gb}^*} E_{ext}. \quad (\text{B.2b})$$

Instead of the number m of small grains contained in the big ellipsoid it is more physical to use the ratio of the total volume of the small ellipsoid to the volume of the basic substance attributable to them, $\mu = m \cdot abc / (ABC)$, where the parameter μ has the meaning of the relative volume fraction of grains. Comparing (B.2a) and (B.2b), we get the following equation for ε_{eff}^* :

$$\frac{\varepsilon_{eff}^* - \varepsilon_{gb}^*}{n_g \varepsilon_{eff}^* + (1-n_g) \varepsilon_{gb}^*} = \frac{\varepsilon_g^* - \varepsilon_{gb}^*}{n_g \varepsilon_g^* + (1-n_g) \varepsilon_{gb}^*} \mu. \quad (\text{B.3})$$

The solution of Eq.(B.3) with respect to ε_{eff}^* is

$$\varepsilon_{eff}^* = \varepsilon_{gb}^* \frac{\{\mu+n_g(1-\mu)\}\varepsilon_g^*+(1-\mu)(1-n_g)\varepsilon_{gb}^*}{n_g(1-\mu)\varepsilon_g^*+\{1-n_g+\mu n_g\}\varepsilon_{gb}^*} = \varepsilon_{gb}^* \left[1 + \frac{\mu(\varepsilon_g^*-\varepsilon_{gb}^*)}{n_g\varepsilon_g^*+(1-n_g)\varepsilon_{gb}^*-n_g\mu(\varepsilon_g^*-\varepsilon_{gb}^*)} \right] \quad (B.4)$$

It is seen that this expression gives $\varepsilon_{eff}^* = \varepsilon_{gb}^*$ and $\varepsilon_{eff}^* = \varepsilon_g^*$ for $\mu = 0$ and $\mu = 1$ respectively, as it should be expected.

For $n_g = 1$ (i.e., for the system consisting of the layers, perpendicular to the external field) one could reduce Eq.(B.4) to the following:

$$\varepsilon_{eff}^* = \left(\frac{1-\mu}{\varepsilon_{gb}^*} + \frac{\mu}{\varepsilon_g^*} \right)^{-1}. \quad (B.5a)$$

It is exactly the result for Maxwell's layered dielectric model.

For $n_g = 1/3$ (i.e., for the system consisting of the spherical grain) one rewrites (B.4) as

$$\varepsilon_{eff}^* = \varepsilon_{gb}^* \left[1 + \frac{3\mu(\varepsilon_g^*-\varepsilon_{gb}^*)}{\varepsilon_g^*+2\varepsilon_{gb}^*-\mu(\varepsilon_g^*-\varepsilon_{gb}^*)} \right], \quad (B.5b)$$

which is the expression derived by the Wagner for the first time.

For $n_g = 0$ (i.e., for the system of the columns, parallel to the external field) one could get the following from of Eq.(B.4)

$$\varepsilon_{eff}^* = (1 - \mu)\varepsilon_{gb}^* + \mu\varepsilon_g^*, \quad (B.5c)$$

which is equivalent to the system with paralleled capacitors of the same thickness but filled with the matters with permittivity values ε_{gb}^* and ε_g^* .

APPENDIX C. Additional figures

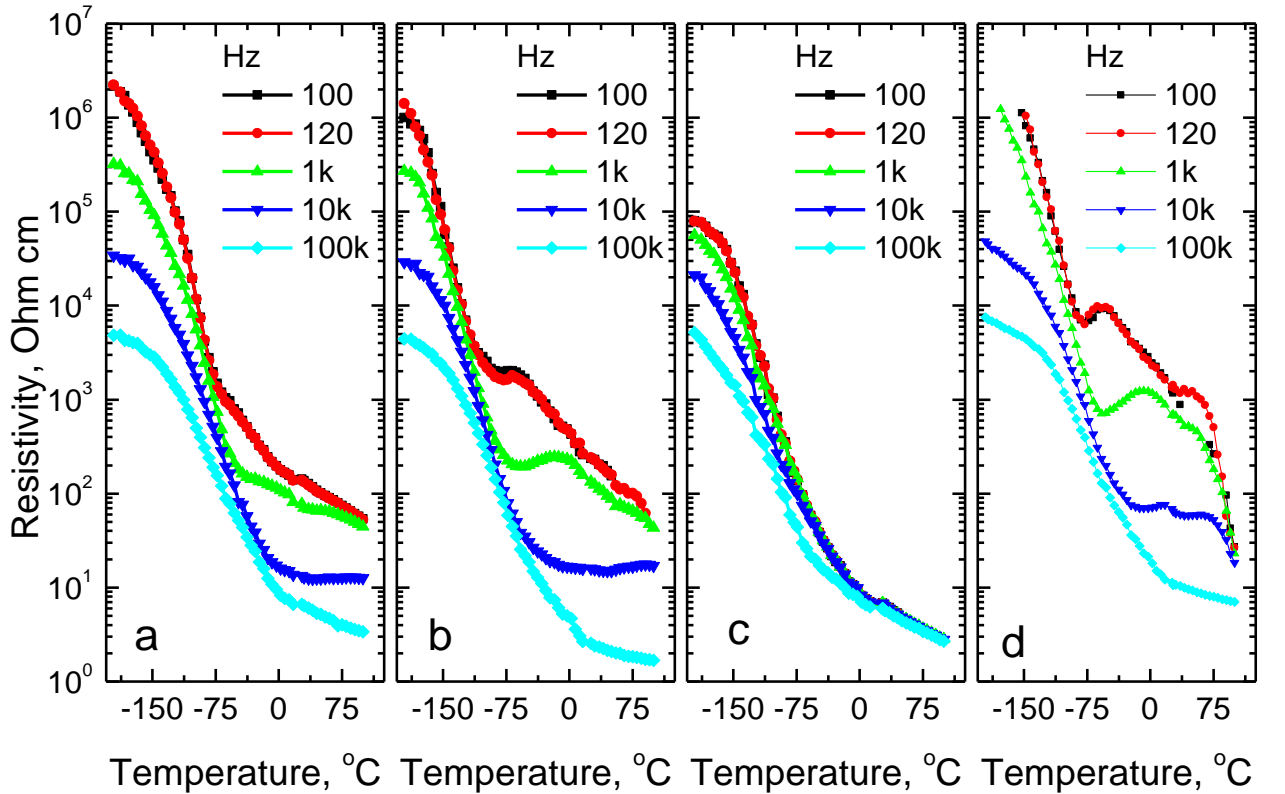


FIGURE C1. The temperature dependences of the resistivity measured for the Samples # 1-4 (a-d) at frequencies from 100 Hz to 100kHz.

References

-
- [1] J. C. Burfoot, G. W. Taylor, "Polar Dielectrics and Their Applications", Macmillan Press: London (1979).
- [2] S. B. Lang, "Sourcebook of Pyroelectricity", London - New York - Paris, Gordon and Breach Sci. Publ., 562 pp. (1974)
- [3] S. Guillemet-Fritsch, Z. Valdez-Nava, C. Tenailleau, T. Lebey, B. Durand, J. Y. Chane-Ching, "Colossal permittivity in ultrafine grain size BaTiO_{3-x} and Ba_{0.95}La_{0.05}TiO_{3-x} materials". Adv. Mater., 20 (3) 551-555 (2008); <https://doi.org/10.1002/adma.200700245>
- [4] M. Tokita, Trends in advanced SPS spark plasma sintering systems and technology. J. Soc. Powder Technol. Jpn., 30(11), 790-804 (1993) (In Japanese); https://doi.org/10.4164/sptj.30.11_790
- [5] H. Maiwa, "Preparation and properties of BaTiO₃ ceramics by spark plasma sintering". Japanese Journal of Applied Physics, 47(9), 7646–7649 (2008); DOI: [10.1143/JJAP.47.7646](https://doi.org/10.1143/JJAP.47.7646).
- [6] M. Tokita, "Progress of spark plasma sintering (SPS) method, systems, ceramics applications and industrialization". Ceramics, 4, 160 - 198 (2021). <https://doi.org/10.3390/ceramics4020014>
- [7] T. Al-Naboulsi, M. Boulos, C. Tenailleau, P. Dufour, M. Zakhour, S. Guillemet-Fritsch, "Colossal and frequency stable permittivity of barium titanate nanoceramics derived from mechanical activation and SPS sintering". International Journal of Engineering Research & Science, 1(7), 25-33 (2015). ISSN 1018-7375.
- [8] M. Tokita, "Method and System for Automatic Electrical Sintering". U.S. Patent No. 6,383,446 B1, 7 May 2002.
- [9] M. S. Jamil, K. E. Saputro, A. Noviyanto, W. B. Widayatno, A. S. Wismogroho, M. I. Amal, N. T. Rochman, T. Nishimura, "Dense and fine-grained barium titanate prepared by spark plasma sintering". International Symposium on Frontier of Applied Physics. IOP Conf. Series: Journal of Physics: Conf. Series 1191 (2019) 012039 doi:10.1088/1742-6596/1191/1/012039
- [10] H. Maiwa, "Preparation and properties of BaTiO₃ ceramics by spark plasma sintering". Japanese Journal of Applied Physics, 47(9), 7646–7649 (2008); DOI: [10.1143/JJAP.47.7646](https://doi.org/10.1143/JJAP.47.7646).
- [11] K.W. Wagner, Arch Elektrotech **2**, 371 (1914); <https://doi.org/10.1007/BF01657322>
- [12] L. Liu, S. Ren, J. Liu, F. Han, J. Zhang, B. Peng, D. Wang, A. A. Bokov, and Z.-G. Ye, Phys. Rev. B **99**, 094110 (2019), <https://doi.org/10.1103/PhysRevB.99.094110>
- [13] See Supplementary Materials for details [URL will be provided by Publisher]
- [14] M. Saleem, M. S. Butt, A. Maqbool, M. A. Umer, M. Shahid, F. Javaid, R. A. Malik, H. Jabbar, H. M. W. Khalil, L. D. Hwan, M. Kim, B.-K. Koo, S. J. Jeong, "Percolation phenomena of dielectric permittivity of a microwave-sintered BaTiO₃-Ag nanocomposite for high energy capacitor", Journal of Alloys and Compounds, **822**, 153525 (2020), <https://doi.org/10.1016/j.jallcom.2019.153525>

-
- [15] Bursian E.V., Girshberg Ya.G., Starov E.N. Small polarons in conducting BaTiO₃ crystals // Phys.stat.solid.(b). –1971. – V.46, No.3. – P.529–533.
- [16] Ihrig H. On the polaron nature of the charge transport in BaTiO₃ // J.Phys.(c). –1976. – V.9, No.18. – P.3469–3474.
- [17] Torsten Granzowa. Polaron-mediated low-frequency dielectric anomaly in reduced LiNbO₃:Ti. Appl. Phys. Lett. 111, 022903 (2017).
- [18] S. L. Bravina, N. V. Morozovsky, A. A. Strokach, “Pyroelectricity: some new research and application aspects”, Material Science and Material Properties for Infrared Optoelectronics, F.F. Sizov (Ed.), v. 3182, pp.85-99, SPIE: Bellingham, (1996).
- [19] S. L. Bravina, N. V. Morozovsky, J. Kulek, B. Hilczer, “Pyroelectric thermowave probing and polarization reversal in TGS/PEO composites”. Mol. Cryst. Liq. Cryst., 497, 109-120 (2008); doi:10.1080/15421400802458761
- [20] A. G. Chynoweth, “Dynamic method for measuring the pyroelectric effect with special reference to barium titanate”. J. Appl. Phys., 27, 78-84 (1956); <https://doi.org/10.1063/1.1722201>
- [21] L. S. Kremenchugsky, *Segnetoelectricheskije Prijomniki Izluchenija (Ferroelectric Detectors of Radiation)*; Naukova Dumka: Kiev, (1971).
- [22] Y. He, “Heat capacity, thermal conductivity, and thermal expansion of barium titanate-based ceramics”. Thermochemica Acta, 419, 135-141 (2004); doi:10.1016/j.tca.2004.02.008.
- [23] E. Kanda, A. Tamaki, and T. Fujimura. "Critical slowing down in the one-dimensional ferroelectric CsH₂PO₄." Journal of Physics C: Solid State Physics 15, no. 15: 3401 (1982). <https://doi.org/10.1088/0022-3719/15/15/012>
- [24] A. N. Morozovska, O. S. Pylypchuk, S. Ivanchenko, E. A. Eliseev, H. V. Shevliakova, L. M. Korolevich, L. P. Yurchenko, O. V. Shyrovkov, N. V. Morozovsky, V. N. Poroshin, Z. Kutnjak, and V. V. Vainberg. Size-induced High Electrocaloric Response of the Dense Ferroelectric Nanocomposites. Ceramics International **50** (7b), 11743 (2024), <https://doi.org/10.1016/j.ceramint.2024.01.079>
- [25] O. Pylypchuk, S. Ivanchenko, Y. Zagorodniy, O. Leschenko, V. Poroshin, O. Bereznykov, M. Yeliseiev. Effective Dielectric Response of Dense Ferroelectric Nanocomposites, Submitted to EL-NANO conference (2024), <https://doi.org/10.48550/arXiv.2401.07311>
- [26] A.N. Morozovska, M.D. Glinchuk, E.A. Eliseev. Phase transitions induced by confinement of ferroic nanoparticles. Phys.Rev. B, **76**, 014102 (2007). <https://doi.org/10.1103/PhysRevB.76.014102>
- [27] E.A. Eliseev, A.N. Morozovska, S.V. Kalinin, and D.R. Evans. Strain-Induced Polarization Enhancement in BaTiO₃ Core-Shell Nanoparticles. Phys.Rev. B. **109**, 014104 (2024), <https://link.aps.org/doi/10.1103/PhysRevB.109.014104>.
- [28] J. Liu, F. Li, Y. Zeng, Z. Jiang, L. Liu, D. Wang, Z. Ye, and C. Jia, Insights into the dielectric response of ferroelectric relaxors from statistical modeling. Phys. Rev. B **96**, 054115 (2017)
- [29] The Mathematica (<https://www.wolfram.com/mathematica>) notebook, which contain the codes, is available per reasonable request.

[30] L.D. Landau, E.M. Lifshitz, L. P. Pitaevskii. *Electrodynamics of Continuous Media*, (Second Edition, Butterworth-Heinemann, Oxford, 1984).

[31] K.W. Wagner, Über dielektrische Nachwirkungsvorärte auf Grund Maxwellscher Vorstellungen. *Archiv für Elektrotechnik*, **2**, 371 (1914). <https://doi.org/10.1007/BF01657322>